Multidimensional Engineering of Perovskites for Optoelectronic Applications

Gaukhar Nigmetova, Bachelor of Science in Chemistry

Submitted in fulfillment of the requirements for the degree of Master of Science in Chemical and Materials Engineering

School of Engineering and Digital Sciences
Department Chemical and Materials Engineering
Nazarbayev University

53 Kabanbay Batyr Avenue,
Nursultan, Kazakhstan, 010000

Supervisors: Chang-Keun Lim, Annie Ng

May 2023

Declaration Form

DECLARATION

I hereby, declare that this manuscript, entitled "*Multidimensional Engineering of Perovskites for Optoelectronic Applications",* is the result of my own work except for quotations and citations which have been duly acknowledged.
I also declare that, to the best of my knowledge and belief, it has not been previously or concurrently submitted, in whole or in part, for any other degree or diploma at Nazarbayev University or any other national or international institution.

Name: Gaukhar Nigmetova

Date: 04.05.2023

Abstract

The importance of perovskite-based solar cells – the emerging materials for photovoltaic applications – heavily relies on the increasing energy demands in recent years. The evolutionary progress has been observed in the area of photovoltaic technologies due to the intrinsic optoelectronic and light harvesting properties that perovskite possesses. In order to address the ambient instability challenges posed to perovskite solar cells, structural modifications of perovskite material are suggested by combining perovskites of different dimensionalities for the solar cell's application. The research on the topic of multidimensionality of dual-halide Cs-based perovskites (i.e., $CsPbI_2Br$) is not conventional and little is reported on the different types of 2D perovskite formation inducing materials suitable for this perovskite system. Most of the reported 2D/3D structures are based on organic and hybrid perovskites, while the inorganic PVKs are limited to $CsPbI_3$. Thus, in this research the main focus is directed towards investigation of intrinsic properties of dual-halide $CsPbI_2Br$ with incorporation of inorganic Cs^+ spacer cation via CsCl post-treatment, which in combination resembles the properties of 3D perovskites incorporated with the 2D structures. The obtained results show that the CsCl post-treatment changes the morphology of perovskite, its composition and crystal lattice, adjusts optical properties as well as improves the performance of the PSC. The obtained champion PSC devices after the post-treatment showed a 48% improvement of the PCE (from 10.9% to 16.2% for the champion PSCs), and maintained stable performance under 20% RH condition.

Acknowledgements

First and foremost, I am profoundly grateful to my supervisors, Annie Ng and Chang-Keun Lim, for their unwavering guidance and professional insight throughout my academic journey, which ultimately led to the successful completion of my MSc Thesis. I am deeply appreciative of the countless hours they dedicated to enriching discussions, their patience and the invaluable advice they imparted, shaping the development of my work.

I would like to express the heartfelt gratitude to my research team and colleagues from other groups, especially to Gulzhan Bizhanova, Zhuldyz Yelzhanova, Damir Aidarkhanov, Alibek Kakimov, Almaz Beisenbayev, and Zhandos Sadirkhanov. Their unwavering support, teamwork and assistantship infused me with the energy and motivation to persevere, nurturing a meticulous and thoughtful approach to research.

To my cherished circle of friends, I extend my warmest thanks for the uplifting companionship they provided during the most challenging moments, and kindly stood by me through peaks and valleys.

Finally, I am deeply grateful to my loving family, who have consistently supported and encouraged me from far away. I constantly receive their endless unconditional love and respect, which have been my guiding star, motivating me forward on this remarkable journey.

Table of Contents

List of Abbreviations & Symbols

EQE	External quantum efficiency
EIS	Electrochemical Impedance Spectroscopy
ETL	Electron Transport Layer
ETM	Electron Transport Material
FTO	Fluorine-doped tin oxide
FF	Fill Factor
HTL	Hole Transport Layer
HTM	Hole Transport Material
I_{SC}	Short-circuit current
I-V	Current-voltage
IQE	Internal quantum efficiency
J_{SC}	Short-circuit density
MPP	Maximum power point
PCE	Power Conversion Efficiency
PL	Photoluminescence
PSC	Perovskite solar cell
SC	Solar Cell
SEM	Scanning Electron Microscope
V_{OC}	Open-circuit voltage
VB	Valence band
XPS	X-ray photoelectron spectroscopy
XRD	X-ray (powder) diffraction

List of Tables

List of Figures

List of Publications

Nigmetova, G., Bizhanova, G., Yelzhanova, Z., Aidarkhanov, D., Pavlenko, V., Lim, C.-K., Jumabekov, A., & Ng, A. (2023). An Effective Interfacial Engineering Method for All-Inorganic $CsPbI_2Br$ Perovskite Solar Cells (in progress).

Bizhanova, G., Pavlenko, V., **Nigmetova, G.,** Ergasheva, Z., Aidarkhanov, D., Ren, Z., Yelzhanova, Z., Parkhomenko, H., Balanay, M., Jumabekov, A., & Ng, A. (2023). An Effective Ionic Liquid-Assisted Crystallization Approach for Fabrication of Highly Reproducible All-Inorganic Perovskite Solar Cells. https://doi.org/10.1039/x0xx00000x (in progress).

Yelzhanova, Z., **Nigmetova, G.**, Aidarkhanov, D., Daniyar, B., Baptayev, B., Balanay, M. P., Jumabekov, A. N., & Ng, A. (2022). A Morphological Study of Solvothermally Grown SnO_2 Nanostructures for Application in Perovskite Solar Cells. Nanomaterials (Vol. 12, Issue 10). https://doi.org/10.3390/nano12101686

Aidarkhanov, D., Ren, Z., Lim, C.-K., Yelzhanova, Z., **Nigmetova, G.**, Taltanova, G., Baptayev, B., Liu, F., Cheung, S. H., Balanay, M., Baumuratov, A., Djurišić, A. B., So, S. K., Surya, C., Prasad, P. N., & Ng, A. (2020). Passivation engineering for hysteresis-free mixed perovskite solar cells. Solar Energy Materials and Solar Cells, 215, 110648. https://doi.org/10.1016/j.solmat.2020.110648

Yelzhanova, Z., **Nigmetova, G.**, Aidarkhanov, D., Maxim, A., Baptayev, B., Balanay, M., Surya, C., & Ng, A. (2020). Optimization of Tin (IV) Oxide Nanostructures Grown by a Solvothermal Method for Perovskite Solar Cells. 2020 47th IEEE Photovoltaic Specialists Conference (PVSC), 1398–1400. https://doi.org/10.1109/PVSC45281.2020.9300951

Ng, A., Ren, Z., Aidarkhanov, D., Yelzhanova, Z., **Nigmetova, G.**, Maxim, A., Akhmetov, B., Fong, P. W. K., Djurišić, A. B., & Surya, C. (2019). Effective Strategies for High Performance Hysteresis-free Mixed Perovskite Solar Cells. 2019 IEEE 46th Photovoltaic Specialists Conference (PVSC), 101–104. https://doi.org/10.1109/PVSC40753.2019.8980784

Chapter 1

Introduction

1.1 Background of Perovskite Solar Cells

In the era of the ever-growing population on the planet and escalating technological progress, the demand on electricity also increases day-by-day, and the research community is challenged to find energy sources which could be both effective and eco-friendly. In light of the evolving trends in emerging photovoltaics, perovskite-based solar cells (PSCs) have captivated experts in the energy materials domain, primarily due to the photophysical and electrical properties that perovskite materials exhibit, along with the promising potential for the implementation of perovskite in optoelectronic applications [1]. Concurrently, PSCs have attracted considerable interest owing to their inherent benefits, such as simplified fabrication, cost-effectiveness, and high efficiency, all of which contribute to their substantial advantages and application potential [2]. Additionally, these solar cells possess efficient absorption of visible light, remarkable charge carrier mobility, and an extended charge carrier diffusion length [3]. In the past decade the PSC field has evidenced a drastic progress in power conversion efficiencies (PCEs), which is set to be a standard criterion to assess photovoltaic devices. Looking at the records from 2009 to 2022 for perovskite-based photovoltaics, the reported PCE underwent an increase from 3.8% up to 25.7% by date [4]. Currently, the PCE of perovskite solar cells precipitously approach the well-established solar cell technologies, including the predominant photovoltaic (PV) systems employing crystalline silicon materials. In laboratory environments without concentrators, these silicon-based PVs have recorded a PCE of 27.6%, which is a sign of comparability between the two technologies in terms of power conversion efficiency [5].

The tunable bandgap is one more advantage of perovskite materials, because aiming to the best energetic alignment the constituent elements within the PSCs can be finely adjusted between electron-transporting material (ETM, or ETL), active layer (perovskite), and hole transporting material (HTM, or HTL) [6]. With perovskite solar cells it is possible to play with the constituent

elements of the crystal lattice, i.e. make perovskite hybrid organic-inorganic ($FAPbI_3$, $MAPbI_3$, where FA - formamidium, MA - methylammonium) and all-inorganic ($CsPbI_3$, $CsPbBr_3$, $CsPbI_2Br$). There is even irregular multication and multianion structures composed crystals, i.e. $Cs_{0.05}(MA_{0.17}FA_{0.83})_{0.95}Pb(I_{0.83}Br_{0.17})_3$. Whereas impressive efficiencies can be achieved by hybrid PSCs, long-term environmental stability is one of the most frequently stated problems for them. For the well-established hybrid perovskite solar cells, which include organic counterparts, such as methylamine and formamidine cations (MA^+ and FA^+, respectively), the thermal stability of perovskite is a major challenge. This instability is primarily attributed to the volatility of the organic components at temperatures starting from 80°C. The thermal instability causes difficulties during the processing of the solar cell fabrication because usually it requires high temperature treatments [7]. To address the issue of thermal instability, the volatile organic components of perovskite are replaced with the inorganic cations such as cesium (Cs^+), which was reported to be a promising component for development of thermally stable all-inorganic perovskites (>350°C) [8] This is a significant step forward in the development of all-inorganic perovskite materials. $CsPbI_3$ is the most well-known Cs^+ perovskite, and it has a narrow bandgap (1.73 eV) that is ideal for solar cell applications. However, there have been numerous reports of $CsPbI_3$ perovskites undergoing phase transitions to a non-photoactive yellow phase (from α phase to δ phase at room temperature) [9]. $CsPbBr_3$ is a more stable alternative, but its high bandgap (2.3 eV) limitates it to absorb low-energy wavelengths (>540 nm) [10]. One way to balance bandgap and stability is to investigate the dual-halide system, which could be equidistant from $CsPbI_3$ and $CsPbBr_3$. The optimal choice is to replace iodine in $CsPbI_3$ with one bromine and obtain $CsPbI_2Br$, which appears to have a little wider bandgap of 1.91 eV than $CsPbI_3$ but also not as high as in $CsPbBr_3$. On top of that, the obtained dual-halide perovskite possesses a more stable cubic phase perovskite compared to the $CsPbI_3$ under ambient conditions [11]. Thus, the $CsPbI_2Br$ perovskite is a promising candidate in PSC applications having advantages in both light harvesting and phase stability. By date, undergoing rapid development, the $CsPbI_2Br$ perovskites have reached 17.1% of PCE [12].

Nowadays, the photovoltaic performance of $CsPbI_2Br$ PSCs is approaching the success of hybrid PSCs, but still for the drastic improvements quality of the perovskite film should be investigated in more details. Although thermal stability is a major advantage of the Cs-based perovskites, the challenge to make them more moisture-tolerant exists till today. Many approaches

are considered to influence the quality of the perovskite active layer, from choosing and optimizing the fabrication technique (one-step-coating deposition [13], vacuum evaporation [14], chemical vapor deposition [15], slot-die coating [16]) to introducing broad range of strategies such as additive engineering [17], post-treatment and interfacial passivation [18], annealing engineering [19].To address the challenge of ambient conditions tolerance, numerous efforts have been undertaken, including employing hydrophobic polymer coatings and incorporating bulk organic cations, with the aim of protecting perovskites from moisture exposure, thereby enhancing the stability and efficiency of associated devices [20]. One of such novel approaches is multidimensional engineering of perovskites which comprise three-dimensional (3D) bulk structures combined together with lower dimensional perovskites. The most common structure of perovskite utilized is 3D hybrid organic-inorganic structures, which suffer from fast degradation mechanisms triggered by water molecules penetration in air or from increased heat transfer. Moving to the topic of crystal alignment of the conventional perovskites, it is becoming clearer that for 3D perovskite crystal lattices the solar cells are barely hitting their ceilings. Contrary to conventional 3D perovskites, lower-dimensional 2D analogs are known for their strong moisture resistance and high temperature tolerance [6]. The reduced dimensionality prevents ion migration processes which is a backbone of the moisture induced degradation. Yet, since 2D perovskites consist of spacer cations, they have less prominent photovoltaic properties due to their insulating nature and decreased charge transfer (electrons and holes transfer), which should be the major driving forces for photovoltaic devices. This is why the 2D perovskites alone are not the best competitors to the 3D perovskites in terms of the aspect of carrier transport mobility. In order to knit the favorable charge-transporting properties of 3D perovskites with stable 2D perovskites, the idea of combination of 3D-2D perovskites was realized and tried in practice [21]. Eventually, incorporation of lower-dimensional perovskites into 3D PSCs was reported to help to overcome instability-caused issues.

1.2 Motivation

The conventional hybrid 3D perovskites being one of the trending structures for photovoltaic applications, however, suffers from fast degradation mechanism due to the weak moisture and thermal stability. The Cs-based perovskites are more promising in terms of thermal stability, while multidimensional engineering is a promising solution for moisture related stability

issues. Among the Cs-based perovskites, dual-halide all-inorganic perovskites are less common, and the solar cell devices optimization with them are altogether least reported nowadays. The proposed procedure consists of obtaining all-inorganic $CsPbI_2Br$ perovskite bulk structure with further optimization of the active layer material with CsCl, which would serve as a Cs^+ spacer cation source to induce 2D perovskite formation. It is a versatile method to provide the solar cell better ambient stability as well as higher photovoltaic performance.

1.3 Aims and Objectives

The aims of the thesis can be divided into two major parts: obtaining uniform polycrystalline perovskite bulk, incorporating CsCl to imply multidimensional interfacial engineering approach, and fabrication of high-performance photovoltaic devices. It is necessary to start approaching these aims by material optimization (Objectives 1-2). Next stage is the device fabrication on the basis of the optimized materials (Objectives 3-4).

Objective 1. To obtain high-crystalline Cs-based 3D-perovskites

Objective 2. To obtain 2D-PVK incorporated with 3D-PVK

Objective 3. To fabricate photovoltaic devices with the integration of 3D-2D structures

Objective 4. To optimize the devices aiming to higher photovoltaic characteristics

1.4 Thesis Outline

The Chapter 2 describes the perovskite solar cell fundamentals starting from the description of perovskite active layer, moving to the multidimensional engineering of perovskites, and ending with the device architecture and working principle of solar cells based on perovskite. Chapter 3 will provide details on the methodology of materials preparation and device fabrication, and give information on the techniques applied to characterize both materials and devices. Chapter 4 demonstrates the findings and observations, and discusses with interpretations each characterization result. The last part of the thesis concludes the results and discussion altogether, and discusses the future plans of the continuous research work.

Chapter 2

Perovskite Solar Cell Fundamentals

2.1 Perovskite crystal structure

Perovskites are the family of materials which exhibit chemical formula ABX_3, where B is an octahedrally coordinated cation, and $[BX_6]^{n-}$ octahedra create a corner-sharing network. A is a large cation (i.e., MA^+, FA^+, Cs^+), and B is commonly a small cation as lead. Meanwhile, X is anion usually is a halogen (I, Cl, Br) (Figure 1) [22]. The ABX_3 structure is characterized by two factors: an octahedral factor (μ) and a tolerance factor (t). The factor t is calculated by dividing the A-X distance by the B-X length. In ideal perovskite geometry, when a solid sphere model is assumed, the formula is as follows [22]:

$$t = R_A + R_X / \sqrt{2} * (R_B + R_X) \quad (1)$$

(where R is the radius of an ion)

Meanwhile, μ is determined as the ratio R_B to R_X. In perovskites, t value is in the range from 0.81 to 1.11, while μ extends from 0.44 to 0.9 [22].

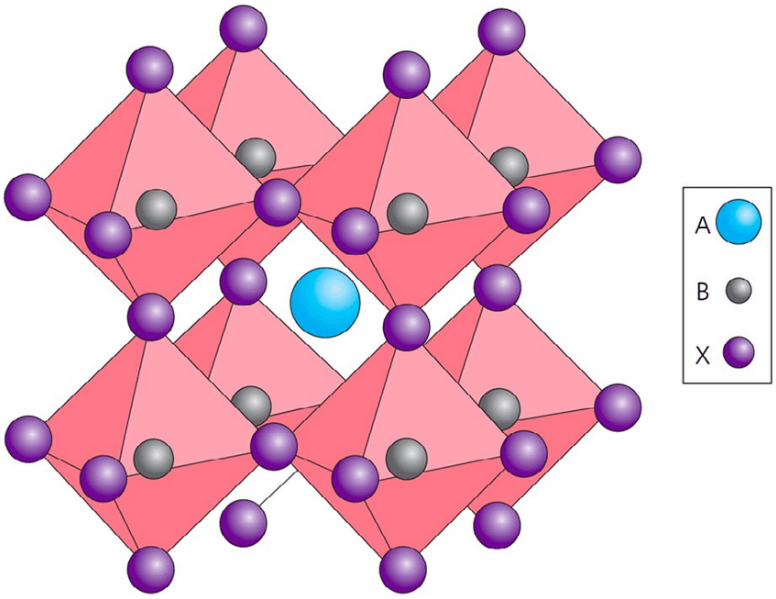

Figure 1. Perovskite crystal structure [22].

2.2 3D-2D Perovskites

The 2D perovskites are obtained by introduction of additional spacer cations (organic cations: phenethylamine [PEA^+], octylamine [OA^+], butylamine [BA^+] etc.; less commonly inorganic ions: cesium [Cs^+]) into 3D perovskite crystals, which intercalate into the crystal lattice, and form either bilayer of the form 3D/2D, or mixed 2D:3D (Figure 2). In the mixed 2D:3D perovskites, the small 2D plates are intercalated in 3D crystals at the surface or grain boundaries, therefore guaranteeing the defect passivation in the 3D bulk layers. In the bilayer 3D/2D perovskites, the 2D cations form a capping layer on top of 3D bulk in the form of ultrathin film [23]. Although the 3D-2D approach at first glance seems to be an ultimate problem-solver, the open questions are still present in the field: how to reduce quantum confinement effect from 2D cations, how to improve interface morphology to reduce any chance of charge recombination etc. [23]. Finding the robust combination of 3D and 2D perovskite materials and proper device engineering is a challenging path in front to achieving high-efficient and stable solar devices.

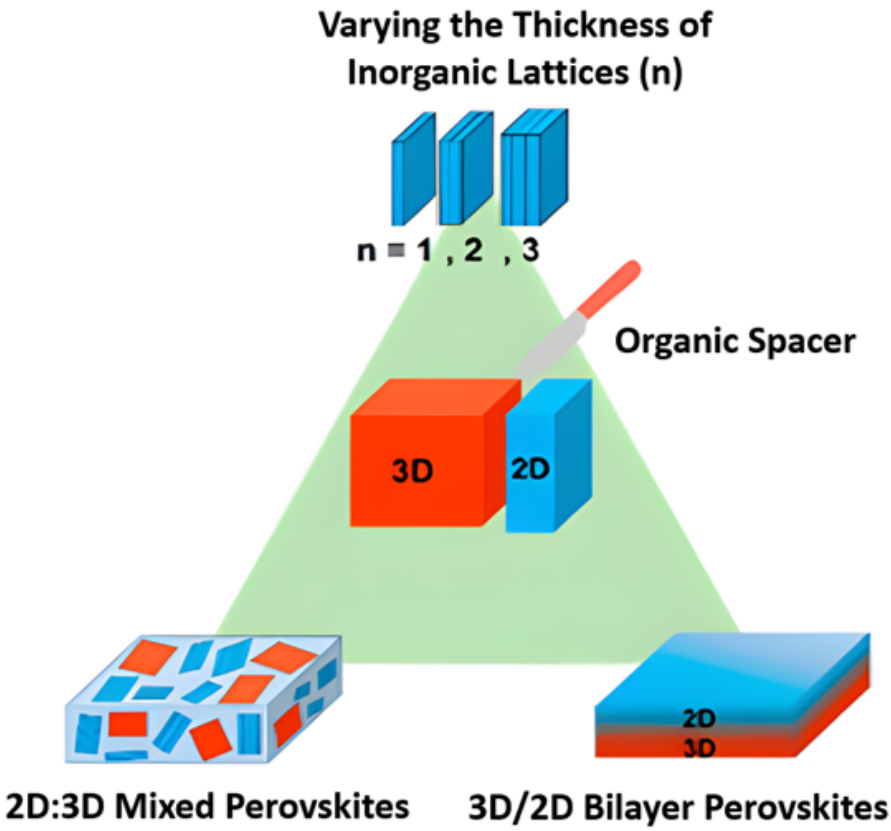

Figure 2. The introduction of organic spacer into 3D bulk structure leads to the formation of either mixed perovskites or bilayer perovskites depending on the method and materials used [24].

The concept of 2D perovskite sandwiched on top of the 3D perovskite was realized by several techniques, and the most popular one is applying long-chain organic cations as 2D precursors. When the 2D precursors with long hydrophobic chains are introduced, the cation of 3D perovskite (FA^+, MA^+ etc.) can be replaced by the new 2D bulky cations, and the 2D A_2BX_4 perovskite is formed.

Y. Liu *et al*. have demonstrated successful synergy of 3D bulk $FAPbI_3$ and 2D agent - pentafluorophenylethylammonium iodide (FEAI). The FEA^+ cation has the advantage of a long-chain organic core and electronegative fluorine, which in combination gives it ultrahydrophobic nature. The FEA^+ cations intercalate into the $FAPbI_3$ 3D crystal and produce the highly moisture-tolerant 2D layer of the form $(FEA)_2PbI_4$. Additionally, the aromatic part of FEA^+ known for its electronic properties provided the additional hole extraction in between of perovskite active layer

and hole-transport layer (HTL). As result, the PCE of the devices increased from 19.97% for regular 3D perovskite to 22.09% for 3D/2D (Table 1). Although the efficiency showed no dramatic change, the lifetime of the 3D/2D solar cells was significantly altered. Due to the enhanced moisture stability after the 1000-h exposure of the solar cells in the atmosphere with a relative humidity of 40%, the control 3D PSC retained only 43% of its initial efficiency, while the 3D/2D PSCs retained 90% of the efficiency [25]. In some cases, the 2D perovskite agent may be a mixture of different organic components. Thus, Y. Cho *et al*. used BAI and FAI mixture to treat 3D organic perovskite. The BAI component has positively affected the surface morphology and hydrophobicity, while the FAI counterpart improved the conduction band alignment with HTL [26].

In inorganic, Cs-based perovskites, 3D/2D architecture is more challenging than for organic/hybrid perovskites, because Cs^+ is less likely to undergo cation-exchange reactions needed for the formation of conventional 3D/2D bilayer. Due to the inability of cesium to participate in 2D capping and cation exchange, the group of Y. Wang *et al*. found an alternative approach - a surface cation termination. In the beginning, they applied PEA^+ cation as an active precursor in different ways (increased concentration, analyzed the XRD and AFM, washed out the PEAI), and evidence suggested the absence of cation exchange reactions between PEA+ and Cs^+, therefore PEA_2PbI_4 2D-layer was not formed. In fact, the only process observed is the physical absorption of PEAI by the surface of $CsPbI_3$, since $CsPbI_3$ is a too robust and rigid structure for any intercalation processes. Instead, the functional groups of PEAI are hypothesized to stabilize the CsPbI3 lattice structure by giving it the proper steric orientations due to the bulkiness of the PEAI molecule. Thus, not only physical rigidity is provided to the active $CsPbI_3$ layer, but also the H_2O penetration is prohibited by the PEAI hydrophobic layer. This is why under relative moisture of 85-90% the - $CsPbI_3$ completely transformed to δ phase rapidly - within an hour, while PEAI-treated $CsPbI_3$ started to degrade only after 24-hour exposure to high moisture [27].

Although it was mentioned that the Cs-based perovskites are highly resistant to external ion penetration into the crystal lattice needed for 2D perovskite formation, in 2021 T. Liu *et al*. found a way to induce it by the excess of PbI_2 on $CsPbI_3$ surface. They created $CsPbI_3/PbI_2$ first, where PbI_2 is accumulated at the grain boundaries of bulk crystals, and then applied organic cation PEA^+. They reported the reaction of the excess PbI_2 with PEAI at the grain boundaries, which

produced PEA_2PbI_4 2D-layer. This layer gave two advantages to fabricated solar cells: 1) passivated grain boundaries, and 2) created a required band gradient for sufficient hole transport [28].

Many of the existing 3D/2D constructions are taking the concept of surface passivation of 3D by 2D precursors. The alternative approaches were taken in applying organic spacer-cations, and one of them suggested by J. Li *et al*. is to construct an inverted structure of PSC (Figure 3c), and deposit PEABr under the active perovskite layer. Thus, contrary to surface passivation, they created the bottom-up passivation effect. PEABr was deposited first, and the $MAPBI_3$ was deposited afterwards. The bottom of the active layer contacts with PEABr, and the defects at the bottom are passivated by means of PEA^+ and Br^- [29].

The other type of perovskites - multiplication and multianion hybrid 3D bulk structures - were also reported to succeed in 3D/2D architecture. For instance, T. M. Koh *et al*. used hybrid 3D $Cs_{0.05}(MA_{0.17}FA_{0.83})_{0.95}Pb(I_{0.83}Br_{0.17})_3$ perovskite, which contained both, organic (FA^+, MA^+) and inorganic (Cs^+) cations, and deposited BAI and OAI on top to form 3D/2D structure. Due to the presence of organic cations (MA^+, FA^+) ready for cation exchange reactions with the BA^+ and OA^+, they obtained an evident 2D layer formed on top of the as-prepared 3D bulk. Additionally, not only structural changes were observed, but also enhanced moisture resistance thus prolonged lifetime of a solar cell was guaranteed (Table 1). Notably, the OA^+ provided the better moisture tolerance to the cell thanks to its hydrophobic nature attributed to the longer alkyl chain [30]. In 2021, another group of M. K. A. Mohammed *et al*. reached exceptional success with hybrid $Cs_{0.05}(MA_{0.17}FA_{0.83})_{0.95}Pb(I_{0.83}Br_{0.17})_3$ perovskites, when treated with the PEAI derivative - 4-Fluoro-Phenethylammonium iodide (4FPEAI) - as a 2D PVK precursor. The 3D absorber crystals were slightly expanded by the means of large $4FPEA^+$, and in result formed 2D $(4FPEA)_2PbI_4$ perovskite top layer, and the state-of-art devices produced the PCE of 19.61% compared to control single-3D - 17.91% [31].

The perovskites of 2D:3D mixed type for simplicity can be divided into two classes: Ruddlesden-Popper (RP) phase and Dion-Jacobson (DJ) phase, depending on the cation type chosen. Basically, RP perovskites utilize monoammonium cations, while DJ perovskites - diammonium cations. Passivation of all-inorganic Cs-based perovskites may undergo the route of

formation of Ruddlesden-Popper (RP) perovskites upon treatment with long-chain monoammonium organic cation sources. One of the good candidates for such organic precursors is PEAI. In 2019, K. Wang *et al*. reported moisture-tolerant and stable 3D:2D Cs-based perovskite, which was obtained after PEAI post-treatment. They aimed to stabilize the black γ-$CsPbI_3$ phase, and it was found that PEA^+ can be a steric hindrance at the crystal growth step, therefore the crystals possess the preferred orientations characteristic to black γ-$CsPbI_3$ phase [32].

More recently, instead of conventional PEAI, another group used the less obvious chemical derivative of PEAI - 4-methoxyphenethylammonium bromide (MOPEABr). The outstanding performance of this type of 2D:3D RP structure was obtained by S. Zhang *et al*., who achieved a PCE of 20.31%. They proposed the spontaneous formation of 2D:3D at room temperature. For this purpose, they post-treated the as-prepared $CsPbI_{3-x}Br_x$ (x = 0.15) with a mixture of MOPEABr/isopropyl alcohol (IPA), and notably, any additional annealing steps were excluded. They observed that the excess of unwanted PbI_2 evident in bulk 3D $CsPbI_{3-x}Br_x$ was eliminated after the bulk film was exposed to MOPEABr treatment, which attributes to the spontaneous reaction of MOPEABr with the PbI_2 [33].

The presence of 2D as a layer between 3D PVK and HTL may result in inhibited upward hole transport. Along with the optimum choice of 2D material, another approach is to engineer the inverted structures (Figure 3c), where the perovskite active layer is in direct contact with hole-transport layer (HTL), and 2D perovskite on top of 3D is exposed to electron-transport layer (ETL). Using this architecture, the hole transfer to HTL is not blocked by 2D material, and on the other hand, 2D material facilitates hole blocking at the interface with ETL, which is a much more favorable scenario. In that sense, Q. Li *et al*. applied BIZI posttreatment on top of CsPbI2Br, obtaining 2D $(BIZ)_2PbI_3Br$ perovskite. The structure was chosen to be inverted - HTL-$CsPbI_2Br$-(BIZI)-ETL. The deposited BIZI not only passivated the surface but also promoted hole blocking and sufficient electron transfer [34].

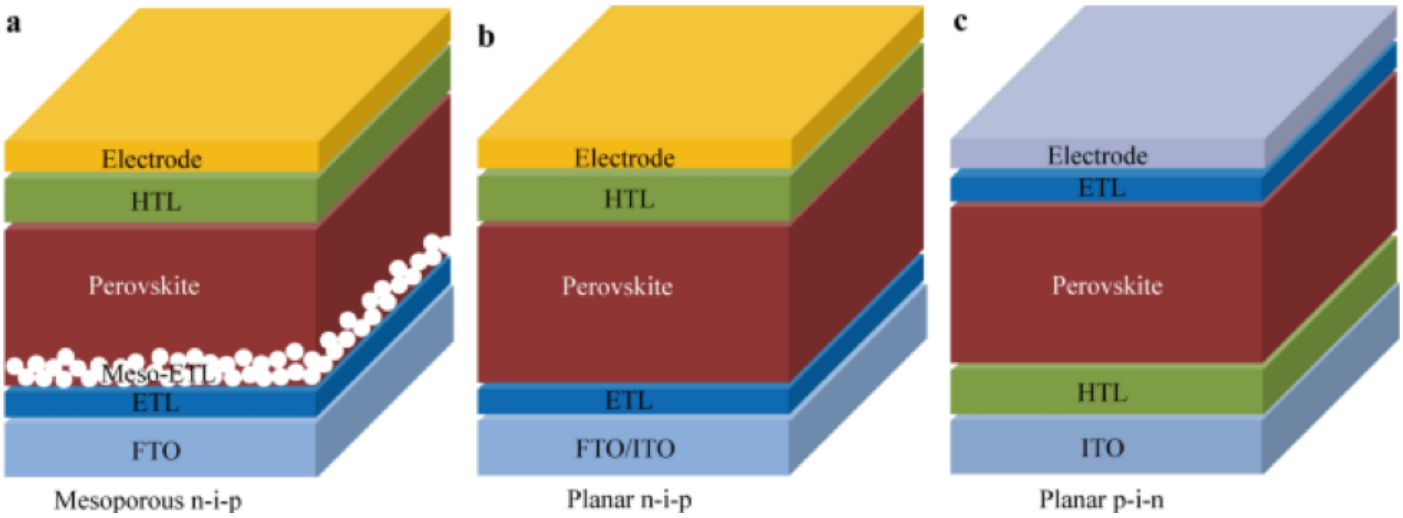

Figure 3. Perovskite solar cells of different structures: (a) mesoporous n-i-p; (b) planar n-i-p (regular); (c) planar p-i-n (inverted) [35].

The all-inorganic Cs-based perovskites were previously reported to be passivated with organic cations, which, in fact, have a drastic size mismatch with Cs^+. The large size mismatch does not provide a smooth energy level gradient needed for effective hole-propagation and electron-blocking, therefore H. Wang *et al*. proposed to post-deposit inorganic 2D precursor such as CsCl, on top of $CsPbI_3$ perovskite. By the addition of CsCl, they induced partial ion-migration between Cl^- of CsCl and I^- of $CsPbI_3$, which created a new Ruddlesden-Popper $Cs_2PbI_2Cl_2$ 2D nanosheets embedded into 3D crystals. The obtained nanosheets provided band level gradient, and additionally acted as an effective electron-blocking layer without the need for hole transporters [36].

Previous to this work, the group of S. Yang *et al*. synthesized $Cs_2PbI_2Cl_2$ 2D nanosheets (NS) in advance and incorporated the obtained nanosheets in two places: on top of ETL and on top of $CsPbI_2Br$ active layer. In general, they sandwiched the active layer in between the NSs, so the heterostructure was in the form of NSs/$CsPbI_2Br$/NSs. This work is specifically focused on the application of as-prepared nanosheets as the novel type of interface engineering of the active layer and the charge-transporting layers (both, ETL and HTL). The bottom-up and top-down simultaneous modification has resulted in enhanced moisture tolerance and suitable aligning of energy levels at the interfaces [37].

Some research works have been focusing on the enhancement of van der Waals interactions between the interfaces, therefore, contrary to the monoammonium RP cations, they suggest diammonium cations. Such cations have ammonia functional groups at both ends of the long-chain organic molecule, and subsequently, induce the formation of Dion-Jacobson (DJ) 2D perovskites. X. Jiang *et al*. have introduced octyldiammonium cation (ODA^+) into 3D perovskite of the form $(FA_{0.85}MA_{0.15})Pb(I_{0.85}Br_{0.15})_3$, and achieved PCE of 21.6%. The ODAI was found to react with the PbI2 excess, creating the capping of the 3D bulk perovskite with enhanced stability under humidity (PCE of 21.6% under a constant relative humidity = 85%) [38]. Similarly, the recent work of the Yukta *et al*. showed that aromatic-core xylylene diammonium iodide (XDAI) organic cation can increase the PCE from 19.6% to 20.74%. They achieved a hydrophobic 2D capping effect, so that for 2D:3D under 60% RH over 1000 h the PCE maintained 80%, while for single 3D PVK it dropped to 35%. In addition, the aromatic nature of XDAI provides an additional hole-promoting effect at the interface of PVK and HTL [39].

However, the problem of hole extraction is still a challenge to this type of 2D:3D heterostructures since large organic spacers hinder the charge transport from perovskite to HTL. To address this issue, W. Li *et al*. introduced a new so-called Localized DJ 2D–3D Heterostructures (L2D–3DH), where they grew the 2D on top of 3D PVK more selectively. They applied 1,4-butanediamine iodide ($BDAI_2$) as post-treatment of the minimal finely-adjusted concentration so that the amount of 2D cations would be as small as to cover the bulk only at the grain boundaries. This method not only opens the space for hole extraction by not covering the full area of 3D bulk but also passivates the 3D crystals at grain boundaries and defenses from H_2O penetration [40]

The summarized data on the performance of solar cells reported in this literature review is given in the Table 1.

Table 1. Power conversion efficiency and stability of 3D-2D perovskite based solar cells.

3D-2D assembling	Perovskite structure (in the form of 3D / 2D)	PCE (%)	Stability (RH, relative humidity)	Reference
3D/2D Bilayer	$FAPbI_3$ / $(FEA)_2PbI_4$	22.09	After 1000 hours: 90% of initial efficiency (RH = 40%)	(Y. Liu *et al*., 2022)
	$CsPbI_3$ / PEA^+	13.5	After 720 hours: 13% of initial efficiency (RH<20%)	(Y. Wang *et al*., 2018)
	$Cs_{0.05}(MA_{0.17}FA_{0.83})_{0.95}Pb(I_{0.83}Br_{0.17})_3$ / BA^+ or OA^+	BA^+: 15.74 OA^+: 15.19	After 100 hours: 86% of initial efficiency (RH>50%)	(T. M. Koh *et al*., 2018)
	$Cs_{0.05}(FA_{0.95}MA_{0.05})_{0.95}Pb(I_{0.95}Br_{0.05})_3$ / 4FPEAI	21.79	After 500 h: 67% of the initial efficiency (RH = 85%)	(M. K. A. Mohammed *et al*., 2022)
	$(FAPbI3)_{0.85}(MAPbBr_3)_{0.15}$ / iBA_2PbI_4	21.7	After 912 hours: >87% of the initial efficiency (RH = 75 ± 20%)	(Y. Cho *et al*., 2018)
	$CsPbI_3$ / PEA_2PbI_4	18.82	After 84 hours: 81% of the initial efficiency (RH = 40 ± 5%)	(T. Liu *et al*., 2021)
	PEA^+ / $MAPbI_3$	19.46	After 1300 hours: 86.1% of the initial efficiency	(J. Li *et al*., 2020)

3D:2D Mixed	$CsPbI_{3-x}Br_x$ / $(MOPEA)_2Pb(Br_xI_{4-x})$	20.15	After 800 hours: 92.3% of initial efficiency (RH = 15-30%)	(S. Zhang *et al*., 2022)
	NS / $CsPbI_2Br$ / NS (NS - $Cs_2PbI_2Cl_2$ nanosheets)	16.65	After 648 hours: >90% of initial efficiency (RH=35%)	(S. Yang *et al*., 2020)
	$CsPbI_3$ / $(PEA)_2Cs_{n-1}Pb_nI_{3n+1}$	13.65	After 288 hours: 89% of the initial efficiency (RH = 25-30%)	(K. Wang *et al*., 2019)
	$(BIZ)_2PbI_3Br$ / $CsPbI_2Br$	14.32	After 336 hours: 95% of the initial efficiency (RH = 15 ± 5%)	(Q. Li *et al*., 2021)
	$CsPbI_3$ / $Cs_2PbI_2Cl_2$	15.23	After 720 hours: 100% of the initial efficiency (RH = 10-20%)	(H. Wang *et al*., 2021)
	$(FA_{0.85}MA_{0.15})Pb(I_{0.85}Br_{0.15})_3$ / $ODAPbI_4$	21.6	After 360 hours: >90% of the initial efficiency (RH = 85%)	(X. Jiang *et al*., 2020).
	$MAPbI_3$ / $(XDA)PbI_4$	20.74	After 1000 hours: 80% of the initial efficiency (RH = 60%)	(Yukta *et al*., 2022)
	$Cs_{0.05}FA_{0.855}MA_{0.095}PbI_{2.7}Br_{0.3}$ / $BDAPbI_4$	20.1	After 1300 hours: 86% of the initial efficiency (RH = 70%)	(W. Li *et al*., 2022)

2.3 Device Architecture and Working Principles

Perovskite solar cells (PSCs) generate electricity through the flow of electrons and holes that are created by the absorption of sunlight. When the perovskite absorber layer is exposed to sunlight, the material absorbs photons, generating excitons, and causing electrons to move to higher energy levels. The electron-hole pairs are separated by the electric field in the solar cell, and upon the separation excited electrons are extracted by the electron transport layer (ETL), while the holes move towards the hole transport layer (HTL) (Figure 4). The ETL and HTL both act as charge transport layers that allow the electrons and holes to move further towards the metal electrodes at either end of the solar cell. In the regular n-i-p device architecture, the bottom electrode collects the electrons, while the top electrode collects the holes. The electrons flow through the external circuit from the bottom electrode to the top electrode, generating an electric current. At the same time, the holes flow from the perovskite layer through the HTL to the top electrode, completing the circuit. The anode and cathode of a perovskite solar cell create a potential difference that drives the flow of electrons from the perovskite material to the external circuit, where they can be used to power devices.

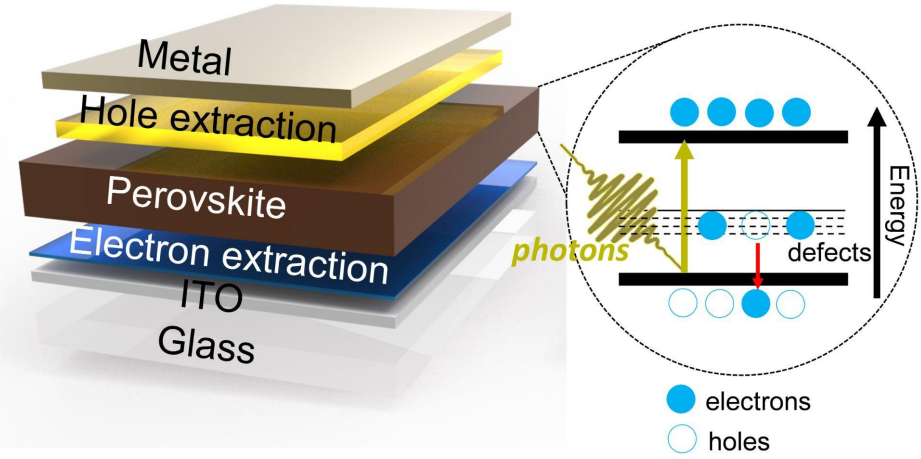

Figure 4. Schematic representation of perovskite solar cell and movement of electron-hole pairs upon radiation [41].

Figure 5 shows the energy level diagram of a perovskite solar cell, explaining the photovoltaic process stages. Initially, light absorption excites electrons from the valence band

(VB) to the conduction band (CB), and in open-circuit illumination there is a nonequilibrium concentration of charge carriers takes place, which leads to the separation of Quasi Fermi levels (EFn and EFp) [42]. The diffusion of photogenerated electrons and holes into the electron and hole transport layers results in charge recombination under open-circuit conditions (Figure 5b) and rapid injection of charge carriers in different directions under short-circuit conditions (Figure 5c).

Ultimately, the shift in EFi gives rise to an electric field that governs the directional movement of charge carriers, consequently generating a current. In this scenario, EFn and EFp converge at the same level, resulting in no output voltage. Under these extreme conditions, the output power of a perovskite solar cell (PSC) is null. However, when the device operates under conditions where both voltage and current are present, as depicted in Figure 5d [42]. The output power of a PSC is nonzero only when the device operates under conditions where both voltage and current coexist, leading to simultaneous recombination and charge transfer.

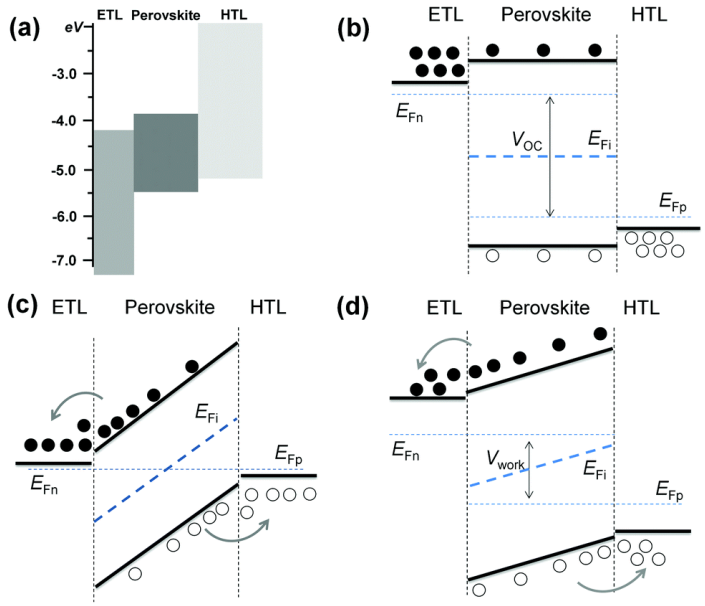

Figure 5. (a) Energy level diagram of PSC; (b) Charge carrier distribution at open circuit; (c) The distribution of charge carriers at short circuit; (d) Charge carrier behavior under the working conditions [42].

In order to establish the proper energy alignment, choice of ETL material usually varies among transparent metal oxides (i.e. ZnO, TiO_2) as they exhibit a proper energy bandgap for Cs-

based perovskites as well as not affecting absorption properties of the photoactive layer. Compact TiO_2 (c-TiO_2), the most common among the mentioned oxides and frequently reported for delivering high efficiency devices, has the limitation in its low electron mobility that leads to inadequate charge separation at the perovskite layer interface. In order to address this issue, one of the strategies involves integrating ZnO as a second ETL above TiO_2, since ZnO is known for its higher electron mobility [43] and lower fabrication temperature as a bonus [44]. Although, it has been reported that hydroxyl groups present in solution-fabricated ZnO films can lead to the deprotonation of organic MA^+ and FA^+ and ultimately the decomposition of organic-inorganic hybrid PSCs [45], this issue does not affect all-inorganic PSCs as they are excluded from organic cations.

The HTL material is comparably of less debates, and the ultimate choice is well-established 2,2',7,7'-tetrakis(N,N-di-p-methoxyphenyl-amine)9,9'-spirobifluorene (Spiro-MeOTAD), which exhibits high hole mobility, enabling efficient transport of holes from the perovskite absorber layer to the anode. Additionally, it has a low tendency to degrade or react with other materials in the device, which facilitates longer lifetime of a solar cell. Finally, its good film-forming ability provides the uniform and smooth HTL layer on top of the perovskite absorber layer, reducing the likelihood of defects and improving charge transport within the device.

Regarding the electrodes in n-i-p planar PSCs, typically, the cathode is a commercially available and widely used in electronics transparent conductive oxide, such as indium-doped tin oxide (ITO) or fluorine-doped tin oxide (FTO). The transparency of the anode is a favourable property as it allows sunlight to pass through the substrate and reach the perovskite active layer. Moreover, ITO and FTO are both relatively stable under conditions during the fabrication and operation of the perovskite solar cell, since the solution processing techniques usually involve high temperatures and chemical solvents that could damage less robust materials. The anode of n-i-p PSCs is a metal, with gold being an optimal choice, not only highly conductive and low-resistant but also stable to corrosion, oxidation, not chemically interacting and disturbing the PSC component layers.

2.4 IV Parameters for Perovskite Solar Cells

The current-voltage (IV) characteristics of devices can offer insights into performance-limiting factors. Nevertheless, owing to the intricate processes within perovskite solar cell (PSC) devices, it is common for multiple performance-limiting mechanisms to coexist. The IV curve of a solar cell represents the superposition of the solar cell diode's IV curve in darkness with the light-generated current (Figure 6). The presence of light causes a downward shift of the IV curve into the fourth quadrant, enabling power extraction from the diode [46].

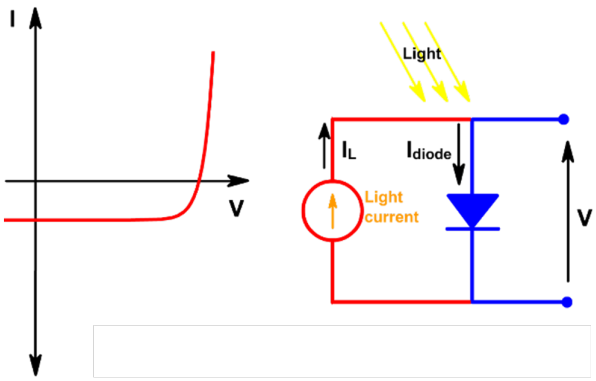

Figure 6. Graphical representation of the short circuit flow of e^- and h^+ at a p-n junction[46].

i) Short-circuit current (I_{SC})

The short-circuit current (I_{SC}) occurs in a solar cell when the voltage is zero, typically when the cell is short-circuited (Figure 7). I_{SC} arises from the generation and collection of carriers induced by light. In an ideal solar cell with moderate resistive loss mechanisms, the short-circuit current and light-generated current are indistinguishable. Consequently, I_{SC} represents the maximum current extractable from the solar cell. The overall performance and efficiency of a solar cell depend on the short-circuit current, which is influenced by several interrelated factors. One of the critical factors is the solar cell area, with larger cells gathering more photons and generating increased current. To ensure a fair comparison between cells of varying sizes, the short-circuit current density (J_{SC} in mA/cm^2) is typically reported rather than the absolute short-circuit current, offering a more precise representation of the solar cell's inherent performance [46].

Another essential factor is the number of photons or the power of the incident light source. Short-circuit current (I_{SC}) is directly proportional to light intensity, with increased light intensity enabling the solar cell to capture more photons and generate higher current. The light intensity on a solar cell is denoted as the number of suns, where one sun corresponds to standard illumination at AM1.5 or 1 kW/m^2. Light intensity not only influences the short-circuit current but also affects open-circuit voltage, fill factor, efficiency, and the impact of series and shunt resistances. The incident light spectrum significantly determines the short-circuit current since solar cells respond differently to various light wavelengths. Consequently, a standardized spectrum called AM1.5 is commonly employed for solar cell measurements, closely simulating Earth's sunlight conditions and enabling consistent comparisons among different solar cells [46].

Additionally, the optical properties of a solar cell, specifically absorption and reflection, play vital roles in determining the short-circuit current. Absorption concerns the solar cell's capacity to capture incident photons and convert them into usable electricity, whereas reflection denotes the loss of photons as they bounce off the cell's surface. Finally, the minority-carrier collection probability substantially affects the short-circuit current, dependent on factors such as surface passivation, which lowers charge carrier recombination at the solar cell surface, and the minority carrier lifetime in the base, which influences the collection time for charge carriers. Optimizing these parameters can result in more efficient solar cells and increased short-circuit currents [46].

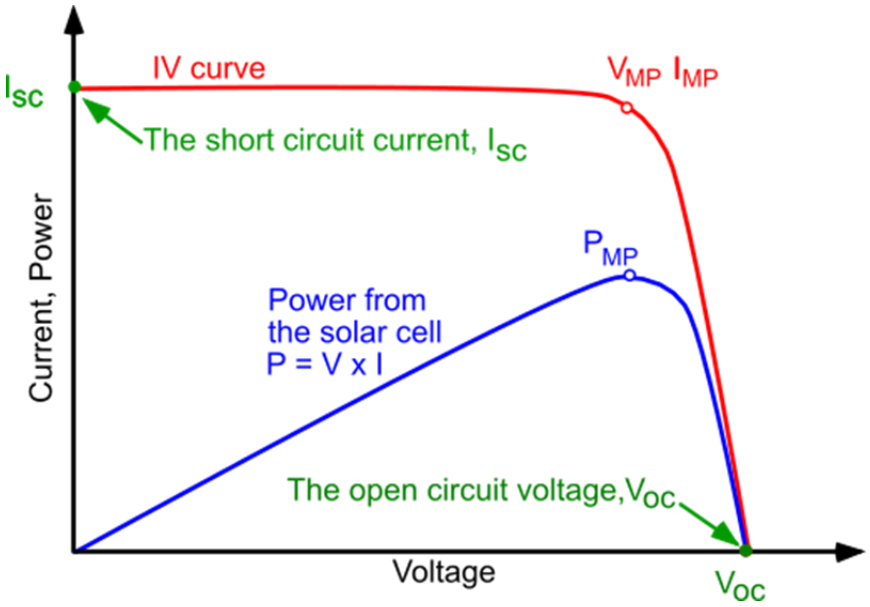

Figure 7. Current voltage (IV) cure of a solar cell [46].

ii) Open-circuit Voltage (V_{OC})

The open-circuit voltage (V_{OC}) represents the maximum voltage attainable from a solar cell, occurring when the current is zero (Figure 7). V_{OC} corresponds to the forward bias imposed on the solar cell due to the solar cell junction's interaction with the light-generated current. V_{OC} relies on the solar cell's saturation current and light-generated current. Although the short-circuit current (I_{SC}) typically exhibits minimal variation, the saturation current is of greater significance, as it may differ by several orders of magnitude. The saturation current (I_0) is contingent upon recombination within the solar cell. Consequently, the open-circuit voltage serves as an indicator of the extent of recombination in the device [46].

iii) Fill Factor

As previously mentioned, the short-circuit current (I_{SC}) and open-circuit voltage (V_{OC}) represent the maximum current and voltage attainable from a solar cell, respectively. Nonetheless, power generation is zero at these operating points. Meanwhile, the fill factor (FF), a crucial parameter used alongside V_{OC} and I_{SC}, determines a solar cell's maximum power. FF is defined as the ratio of the solar cell's maximum power to the product of V_{OC} and I_{SC}, which serves as an indicator of the IV curve's "squareness.":

$$FF = \frac{P_{MP}}{V_{OC} \times I_{SC}} \quad (2)$$

A higher voltage solar cell has a larger potential FF due to the reduced area of the IV curve's "rounded" portion (Figure 8) [46].

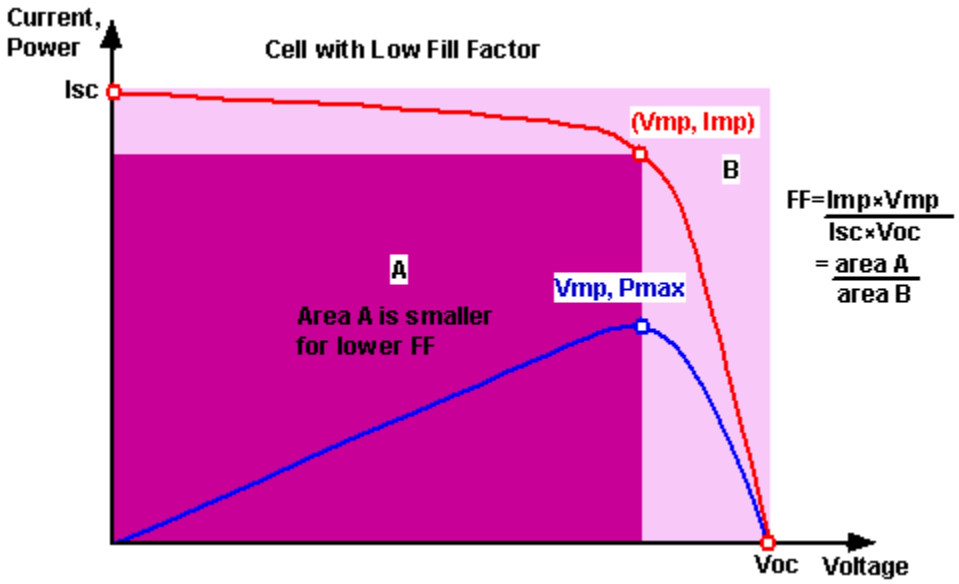

Figure 8. Graphical representation of the FF in the IV curve [46].

One of the primary factors affecting FF is recombination processes occurring within perovskite solar cell (PSC) component layers. Recombination removes a hole when an electron stabilizes into the valence band. Radiative and nonradiative recombination are two types that occur in solar cells. Radiative recombination involves an electron from the conduction band directly combining with a hole in the valence band, releasing a photon with energy similar to the band gap. Nonradiative recombination occurs when an electron or hole trapped in a defect or impurity recombines with a hole or electron in the perovskite's valence or conduction band [46]. In polycrystalline perovskite thin films, defects or impurities are likely concentrated at grain boundaries (GBs) and film surfaces. While nonradiative recombination at interfaces influences PSC performance, GBs' role in device performance remains debated [47].

Parasitic resistances, such as series resistance (R_S) and shunt resistance (R_{SH}), also are the reasons for changing FF (Figure 9). Resistive effects in solar cells reduce efficiency by dissipating power in resistances. Series resistance (R_S) can originate at interfaces between the perovskite layer and

adjacent layers (ETL, HTL), with imperfections or impurities leading to increased contact resistance and hindered charge carrier transport. The ETL, HTL, perovskite material resistance, and electrode resistance also contribute to the overall series resistance. Conversely, significant power losses due to low shunt resistance (R_{SH}) are typically attributed to manufacturing defects rather than poor solar cell design. Low shunt resistance causes power losses by providing an alternate current path for light-generated current, reducing the current flowing through the solar cell junction and the voltage from the solar cell [46].

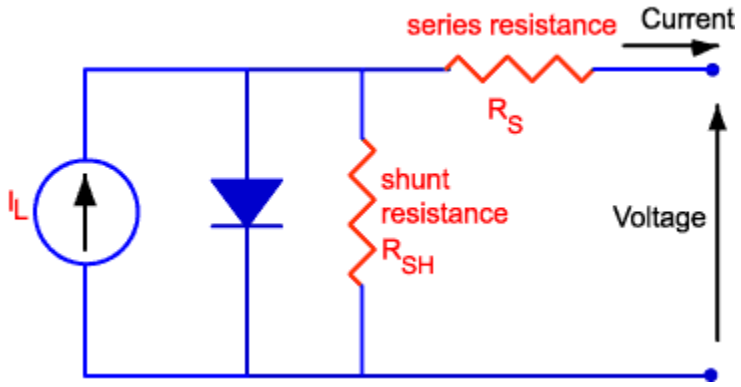

Figure 9. Series and shunt resistances (R_S and R_{SH}) in a solar cell circuit [46].

Chapter 3

Methodology

3.1 Materials preparation

i) Electron-transport layer (ETL)

Prior to the deposition of ETL materials, the fluorine-doped tin oxide (FTO) coated glass substrates were preliminarily prepared. The FTO-coated glass substrates were sequentially cleaned with isopropanol (IPA), and sequential sonication in detergent included water, distilled (DI) water, acetone, and IPA for 15 min in each solvent, by two rounds. After the substrates are cleaned, they are dried under direct N_2 flow, followed by UV-ozone treatment for 20 min. The TiO_2 ETL precursor solution is pre-synthesized from TTIP, IPA, PVP and acetic acid. First, 150 mg of polyvinylpyrrolidone (PVP) was dissolved in IPA (6.25 mL) and acetic acid mixture (1.25 mL). Next, the mixture was gradually added to the mixture of IPA (6.25 mL) and TTIP (1.25 mL). Finally, the solution was diluted in the additional 15 mL of IPA.

The second layer of ETL composed of ZnO ink solution, which was filtered and ultrasonicated for 15 minutes before the deposition.

ii) Perovskite active layer

The perovskite precursor was prepared by dissolving 0.9 M CsI, 0.45 M PbI_2, and 0.45 M $PbBr_2$ in DMF:DMSO solvent mixture (4:1, 1 mL). The solution was stirred in a vortex mixture for 12 hours to dissolve all components in an N_2 glove box. The CsCl solutions were prepared with by dissolving CsCl crystals in IPA (0.45 M).

iii) Hole-transport Layer (HTL)

The Spiro-MeOTAD solution for HTL was prepared by dissolving 40 mg of Spiro-MeOTAD powder in 0.5 mL of chlorobenzene (CB), 14.5 µl of TBP, and 9 µl of lithium (Li) salt. The Li salt was prepared by adding 520 mg of LiTFSi to 1 mL of acetonitrile.

iv) Device Fabrication

The pre-TiO_2 solution was spin-coated (3000 rpm, 3000 rpm/s, 30 sec) on FTO-glass (70 μL), followed by a sintering step at 500°C for 2 hours for obtaining c-TiO_2 single layer. After the substrates were cooled down to room temperature, the second layer of ETL was deposited: 70 μL of ZnO ink solution was spin-coated on top (3000 rpm, 3000 rpm/s, 30 sec), and annealed at 110°C for 10 min. Then, the double-layer ETL-covered substrates were put to the UV-ozone treatment.

The $CsPbI_2Br$ film was fabricated by spin-coating perovskite precursor solution (70 µL) at 1000 rpm for 10 s and 5000 rpm for the 30 s. The films were annealed on a hotplate at 40 °C for 2 min and 250 °C for 10 min to complete the crystallization of perovskite film. For obtaining CsCl-treated $CsPbI_2Br$ perovskites, 70 µL of CsCl in IPA solution (0.45 M) was spin-coated at 5000 rpm, 5000rpm/s, 20 sec on top of the pristine as-prepared $CsPbI_2Br$ perovskite. For the different CsCl treatment duration, the time of loading of the CsCl before the spin-coating step was varied from 10 seconds to 5 minutes. Then, the substrate was annealed under 100°C for 10 min.

The Spiro-MeOTAD-based HTL was deposited on top of the as-prepared perovskite by spin-coating the Spiro-MeOTAD solution at 3000 rpm, 2500 rpm/s for 30 sec.

The gold electrodes were thermally evaporated on the HTL layer under the vacuum of 10^{-6} Torr, and had the final thickness of 70 nm.

3.2 Materials Characterization

i) X-Ray Diffraction (XRD)

X-ray powder diffraction (XRD) is used to determine the crystallographic characteristics of a target material or identify the crystalline materials. The observation is based on their unique

atomic structures, and in order to investigate the material in an atomic level, the x-ray radiation is used. The X-rays interact with crystal lattices, and the XRD analytical approach gives information on the crystallographic planes of a material which has a specific atomic ordering. The working principle of the XRD instrument starts from the source emitter - X-ray tube. The tube generates X-rays by bombarding a target material, often made of metals such as copper, molybdenum, or chromium, with high-energy electrons. The electrons are typically accelerated by applying a high voltage across the tube. When the accelerated electrons strike the target material, they cause the emission of X-rays due to the interaction between the electrons and the target atoms. The emitted X-rays are then used to illuminate the sample under investigation in the XRD analysis. The scattered rays then reach the detector, and the angle between the incident and diffracted rays is recorded, and denoted as θ. Constructive interference occurs when the top and bottom wave-paths coincide, resulting in a peak on the XRD spectrum. Conversely, destructive interference occurs when the paths do not align, leading to an absence of peaks in the diffractogram. To achieve constructive interference, the lower wave-path must travel an additional distance, denoted as λ. By considering the information about θ, λ, and the interplanar distance (d-spacing), and applying geometric principles, λ can be equated to the following formula according to the Bragg's Law [48]:

$$n\lambda = 2d(\sin\theta) \tag{3}$$

For XRD measurement, a sample of perovskite thin film on top of the FTO-glass substrate was put in the fixed chamber on a sample holder of the XRD System (SmartLab Rigaku). In the SmartLab Studio II software the angle range was set to be from 10° to 40°, speed duration time at 3.5, data acquisition mode - 1D, the monochromatization method is K beta filter, voltage 40 kV, and current 30 mA. Additionally, the optics alignment was chosen to be Bragg-Brentano focusing. Throughout the analysis, first, the optics alignment was completed, then the sample allignment was started. After the alignment steps were finished, the measurement started, the source and detector's positions were simultaneously changing, increasing the θ angle. Upon completion, the raw data was saved, and the X-ray source and detectors returned to their original positions.

ii) Scanning Electron Microscopy (SEM)

Scanning electron microscopy is an imaging technique that gives information about topography and chemical composition of a sample material from its scattered electrons and X-rays. SEM benefits from optical microscopy by the allowed resolution and magnification of the image. It can spatially resolve objects as small as 20 nm, and magnification can be as large as 3´106 times. It also allows not only to see the topography of a sample but also conduct qualitative analysis of chemical composition of a specimen, assess thickness of coatings, measure dimensions of nano-scaled objects. However, the energy dispersive X-ray spectrometry (EDS) is not that powerful compared to other types of spectroscopy techniques [49].

The principle of SEM is based on the effect of electron scattering from the surface of a sample material. In order to eject initial electrons with high enough energy, the source of some material (i.e. tungsten filament) is heated, and a beam is generated. The path electron beam needs to be precisely controlled, and for this purpose, they firstly go through positively-charged anode, which deflects electrons so that they fly in a specific direction. During the process, vacuum conditions are required, since the molecules in air may obstruct the straight path of electrons. Next, the path of electrons is controlled by electromagnetic lenses, which are basically coils of wires that undergo current. Here a magnetic field is generated, and the adjusted effect of the magnetic field can create a desired path of electrons. The condenser is an electromagnetic lens that converges the beam and adjusts the size of the beam - this is how resolution can be achieved. Objective lens is another type of electromagnetic lens which also converges the beam by helping to create a desired focus on the specimen. The scanning of the specimen surface is done in a raster pattern, which is achieved by scanning coils [49]. The electrons are scattered from the surface of a specimen, and finally collected by detectors.

There are three detectors: one collects backscattered electrons (BSE), another - secondary electrons (SE), third - X-rays. BSEs are the incident electrons which return back as a result of elastic scattering between the incident electrons and a specimen material. It gives information about different atomic numbers over the scanned region in the way that the heavier elements, the brighter it is shown in image. SEs come from the atoms of a specimen material after incident electrons “kick out” the inner electrons. They give information about the surface of a material, and

are most responsible for 3D image. X-rays are also detected by SEM, which is useful for energy dispersive x-ray spectrometry (EDS). Using X-rays it becomes possible to identify elemental composition of a specimen. From detectors the collected signals are then converted into image and displayed on a PC monitor. The equipment used in this methodology is SEM Crossbeam 540 (Zeiss).

Sample preparation and data acquisition:

1) Perovskite-coated samples were sputtered with 4 nm of gold in order to make the top and cross-sectional surfaces more conductive;
2) Samples were attached to the multi-holder on top of pin stubs by carbon tape. The pin stubs were tightened to the holder before putting it into the sample chamber. Sample chamber and the SEM column were vacuum sealed;
3) The sample holder was closely adjusted under the beam booster, and the analysis was started;
4) Column mode was set to either “Analytic”; EHT = 5kV; WD = 3.8 mm; Scan Speed = 4; I Probe = 100 pA. The obtained images were saved.

iii) Atomic Force Microscopy (AFM)

Atomic Force Microscopy (AFM) is a high-resolution imaging technique that allows for the visualization of surfaces at the atomic level. It operates based on the interactions between a sharp probe tip, mounted on a flexible cantilever, and the sample's surface. The working principle of AFM involves three key components: a sharp probe tip, a cantilever, and a detection system. The probe tip, usually made of silicon or silicon nitride, is attached to a flexible cantilever. The tip is brought close to the sample surface, and the interatomic forces between the tip and the surface cause the cantilever to deflect [50]. There are several modes in which AFM can operate, but the two most common modes are contact mode and tapping mode. In this mode, the probe tip maintains constant contact with the sample surface. As the tip is scanned across the surface, the interatomic forces cause the cantilever to bend. A feedback loop is used to maintain a constant deflection, which corresponds to a constant force between the tip and the surface. By monitoring the vertical movement of the probe needed to maintain this constant force, a topographical map of the surface is generated. In tapping mode, the cantilever is oscillated at or near its resonance frequency. As

the probe tip approaches the surface, the oscillation amplitude is reduced due to the tip-sample interactions. A feedback loop is used to maintain a constant amplitude, which corresponds to a constant force between the tip and the surface. By monitoring the vertical movement of the probe needed to maintain this constant amplitude, a topographical map of the surface is generated [50].

The detection system, usually based on a laser and a position-sensitive photodiode (PSPD), measures the deflection or oscillation amplitude of the cantilever. A laser beam is directed onto the back of the cantilever and reflected onto the PSPD. As the cantilever bends or oscillates due to tip-sample interactions, the laser spot on the PSPD moves, providing a measurement of the cantilever's movement [50]. The data obtained from the detection system is processed to generate a high-resolution, three-dimensional topographical image of the sample surface. The equipment used in this methodology is Atomic Force Microscope SmartSPM 1000, the software is Qscan. The samples were scanned at ptsX and ptsY = 512 referring to the scan size in x and y directions.

iv) X-Ray Photoelectron Spectroscopy (XPS)

X-ray photoelectron spectroscopy (XPS) is a method to investigate surface chemistry (up to 10 nm), which yields information on the elemental composition and their corresponding chemical states. During XPS analysis, X-ray beams coming from a monochromatic source such as a magnesium or aluminum anode are bombarded on the surface of a sample, they ionize the atoms in the outermost layer, causing the emission of photoelectrons [51]. The energy of the emitted photoelectrons is characteristic of the chemical bonding state of the atoms from which they were emitted, and electron energy analyzer measures the kinetic energy of these photoelectrons. The binding energy (BE) can be calculated using the equation:

$$BE = h\nu - KE \tag{4}$$

where hv represents the energy of the X-ray. Changes in the binding energy of a photoelectron are caused by the chemical surroundings of an atom, leading to variations in the measured kinetic energy (KE) [51]. By analyzing chemical shifts, it is possible to obtain information about the chemical interactions in the material. For $CsPbI_2Br$ perovskites, the targeted elements and corresponding orbitals are Cs 3d, Pb 4f, I 3d, Br 3d.

v) Photoluminescence Spectroscopy (PL)

Photoluminescence (PL) spectroscopy is a non-destructive optical technique used to characterize the properties of semiconductor materials such as bandgap, defect states, and carrier lifetime. It involves the excitation of a material with a light source (such as a laser) to create electron-hole pairs, followed by the recombination of these pairs, which results in the emission of light (photoluminescence). The emitted light's spectral distribution and intensity provide information about the material's electronic and structural properties [52].

Perovskite material is prepared on a glass substrate, and placed on a sample holder special for thin films. A monochromatic light source, usually a continuous-wave or pulsed laser, is used to excite the perovskite material, inducing the energy of the incident photons greater than the bandgap of the material, which enables the promotion of electrons from the valence band to the conduction band, creating electron-hole pairs. After the excitation, the excited electrons and holes in the material recombine either radiatively (photons) or non-radiatively (phonons). Radiative recombination results in the emission of photons (photoluminescence), while non-radiative recombination dissipates the energy as heat. The photoluminescence signal is directly related to the efficiency of radiative recombination. The emitted photoluminescence signal is collected using optical components such as lenses or mirrors, and is then focused onto a spectrometer. The spectrometer disperses the collected light according to its wavelength, allowing for the analysis of the emitted light's spectral distribution [52]. In current experiments the important region to analyze the PL is 550-750 nm, since in this range a peak appears corresponding to the bandgap energy of typical Cs-based perovskites.

To confirm the presence of defect states and construct more detailed map about their nature, it is beneficial to correlate the PL data with other characterization techniques such as deep-level transient spectroscopy (DLTS), electron paramagnetic resonance (EPR), or X-ray photoelectron spectroscopy (XPS). These techniques can provide complementary information about the type, concentration, and energy levels of the defect states, allowing for a more comprehensive understanding of perovskite quality.

vi) UV-Visible Spectroscopy (UV-Vis)

UV-Vis spectroscopy is a technique for characterizing the optical properties of perovskite materials such as its absorption, transmission, or reflection of light in the ultraviolet, visible, and near-infrared spectral regions as a function of wavelength. One of the key parameters obtained from visible spectroscopy is the absorption coefficient, which provides information about the material's bandgap and the efficiency of light absorption in the solar cell [53]. After the sample is placed in a UV-Vis spectrophotometer, the spectrophotometer measures the absorption in a range of 500-800 nm, since for Cs-based perovskites it is the most valuable region to evaluate energy bandgap. The spectrophotometer uses a light source (a combination of tungsten or halogen lamp for the visible range) to illuminate the sample. The absorbed light is collected and directed to a detector, which measures the light intensity as a function of wavelength. Next, the spectrophotometer records the light intensity at each wavelength and calculates the absorbance spectrum of the sample. The absorbance spectrum (A) is particularly important for determining the material's optical properties, such as the absorption coefficient (α) and the bandgap (Eg) [53].

To determine the bandgap of the perovskite material from the absorption spectrum, Tauc plot is used, where the absorption coefficient can be calculated from the absorbance (A) using the Beer-Lambert law:

$$\alpha = A / d \tag{5}$$

where d is a thickness of the film

Then, the photon energy (hν) is found by converting the wavelength of the absorption spectrum to photon energy using the equation:

$$h\nu = hc / \lambda \tag{6}$$

(where h - Planck's constant, c - speed of light, and λ - wavelength). The Tauc plot is then plotted as a graph of $(\alpha h\nu)^2$ versus the photon energy (hν). In the Tauc plot, the linear region corresponds to the material's absorption edge, and by extrapolating this linear region back to the photon energy axis ($\alpha h\nu = 0$), the value at the intersection point with the photon energy axis represents the bandgap (E_g) of the material.

3.3 Device Characterization

i) Current-voltage characteristics (I-V)

The current-voltage (I-V) characteristics of a perovskite solar cell describe the relationship between the current generated by the device and the voltage applied across its terminals. I-V measurements are crucial for evaluating the performance and efficiency of solar cells, as they provide key parameters such as the short-circuit current (I_{SC}), open-circuit voltage (V_{OC}), fill factor (FF), and power conversion efficiency (PCE) [46]. The light I-V curve is particularly relevant for evaluating the solar cell's performance when converting sunlight into electrical energy, therefore the measurements were performed using a Keithley 2440 source meter under the AAA class ORIEL Sol3A solar simulator equipped with an AM 1.5G filter at 100 mW/cm^2. The samples were measured under the aperture of the distinct diameter of 1.2 mm^2.

After the light is illuminated on the back side of the PSC, the maximum current generated by the solar cell when the voltage across the terminals is zero (V=0) corresponds to the I_{SC} value. It represents the total amount of photogenerated current in the solar cell, and it is directly proportional to the incident light intensity and the cell's ability to absorb and convert photons into charge carriers. The open-circuit voltage (V_{OC}) is the voltage across the solar cell's terminals when no current flows through the external circuit (I=0). It is an indicator of the built-in electric field in the solar cell and is influenced by factors such as the bandgap of the perovskite material, carrier recombination, and the quality of the interfaces between different layers in the device. The maximum power output (P_{max}) that the solar cell can deliver to the external circuit is a product of the current (I_{max}) and the voltage (V_{max}) at this specific point on the curve, and is called maximum power point (MPP). One more important characteristic is a fill factor, which is a measure of the solar cell's "squareness" or the quality of the I-V curve. It is defined as the ratio of the maximum power output (P_{max}) to the product of the short-circuit current (I_{SC}) and open-circuit voltage (V_{OC}) [46]:

$$FF = P_{max} / (I_{SC} \times V_{OC}) \quad (7)$$

Ideal FF has a value of 1, and corresponds to the I-V curve which is a perfect square-shape. In reality, such behaviour of the I-V curve does not appear, therefore typical FF has a value of less

than 1. However, FF can be compared between the control and optimized devices, and the higher value indicates a more efficient solar cell, as it signifies reduced resistive losses and better charge extraction. Finally, the key performance metric of PSCs and a major evaluation criteria to aim for - power conversion efficiency (PCE). It is defined as the ratio of the maximum power output (P_{max}) to the incident light power (P_{in}): PCE = P_{max} / P_{in}. The PCE takes into account the short-circuit current (I_{SC}), open-circuit voltage (V_{OC}), and fill factor (FF) and provides a comprehensive measure of the solar cell's ability to convert sunlight into electrical energy [46].

ii) Quantum efficiency (QE)

Quantum Efficiency (QE) is an important parameter for evaluating the efficiency of a solar cell in converting absorbed photons into charge carriers that contribute to the photocurrent. IQE takes into account the losses within the solar cell, such as carrier recombination and incomplete charge extraction. It is closely related to the External Quantum Efficiency (EQE), which measures the efficiency of the solar cell in converting incident photons into photocurrent [54]. EQE is the ratio of the number of charge carriers collected by the solar cell's contacts to the number of incident photons at a specific wavelength. To measure EQE, a monochromatic light source is used to illuminate the solar cell with light of varying wavelengths. Here the chosen range for $CsPbI_2Br$ perovskites is between 300 nm and 750 nm. The photocurrent generated by the solar cell is measured as a function of the incident light wavelength, and the EQE spectrum is obtained by normalizing the photocurrent with respect to the incident photon flux. EQE gives a general map of information about reflection losses, incomplete light absorption, carrier recombination, and inefficient charge extraction, while IQE focuses on the processes that occur within the solar cell after light absorption (charge generation, separation, and collection) [54].

Chapter 4

Results and Discussion

4.1 Scanning Electron Microscopy (SEM) and Atomic Force Microscopy (AFM)

To study the morphological and topographical properties of perovskite, the top and cross-sectional SEM images were obtained demonstrating the perovskite thin film before and after CsCl treatment (Figure 10). The obtained perovskite layer has a smooth surface morphology with low density of defects, and the large grain size exceeding 1.5 μm. The top and the cross-sectional views show that the surface coverage is uniform and without pin holes. Large grain size and uniform surface coverage of the perovskite layer lowers the chances of non-radiative recombination and charge carrier trapping effect within the perovskite layer, which plays a significant role in enhancing the power conversion efficiency of PSCs.

From the top view the morphology undergoes changes after CsCl treatment depending on duration of the treatment (Figure 10 b-c). It becomes evident that upon CsCl treatment the bulk pristine perovskite obtains additional structure of a distinct morphology in the form of nanoneedles, which densifies under the longer treatment with CsCl. The further investigated cross-sectional images show the protruded “rod”-like vertically-oriented structures identified on samples after treatment with CsCl (Figure 10e). It can be concluded that these artifact structures are the results of the induced morphological changes due to the CsCl introducing the perovskite bulk.

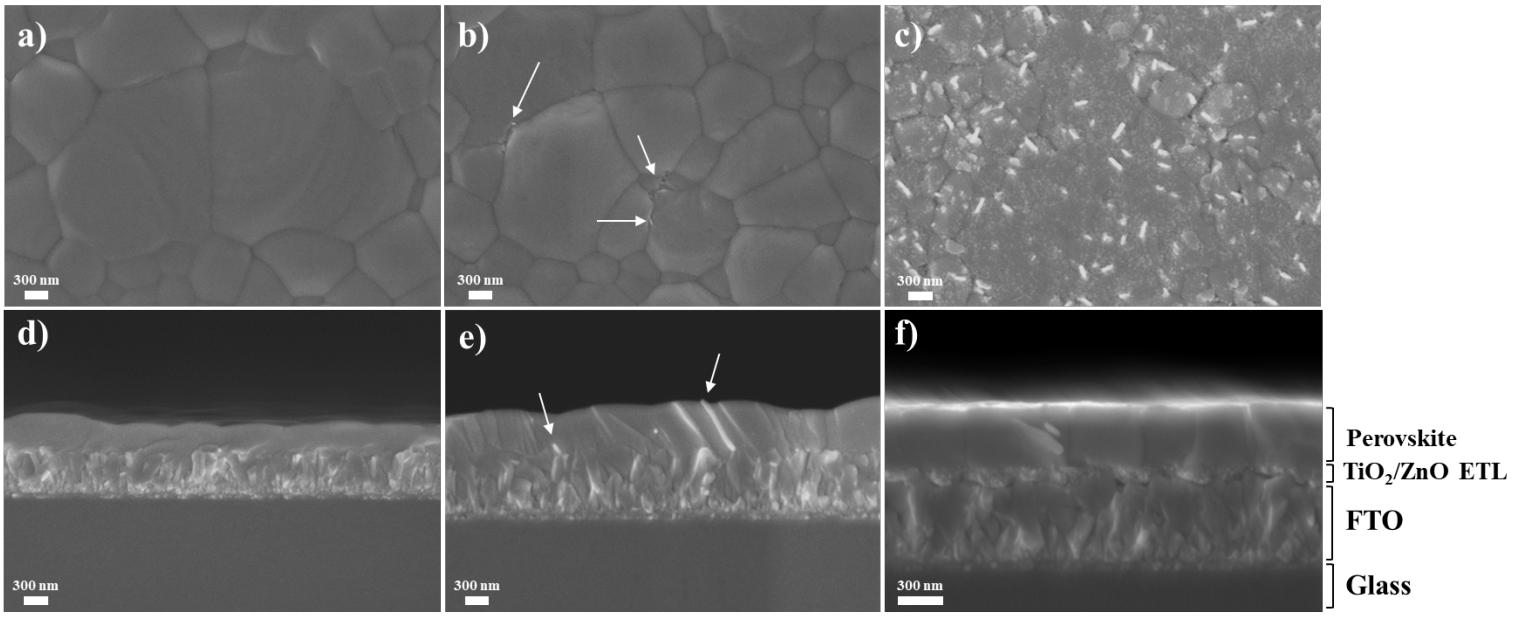

Figure 10. SEM images of top and cross-sectional view on $CsPbI_2Br$ perovskite crystal (a,d)without CsCl, (b,e)with CsCl post-treatment (10 sec), (c)with CsCl post-treatment (5 min); (f) cross-sectional view on perovskite on top of TiO_2/ZnO ETL.

Figure 10f shows the cross-sectional SEM image of the perovskite deposited on top of the TiO_2/ZnO ETL, and there is an evident separation between the ETL and perovskite implying that both of the layers co-exist with no drastic effect on the perovskite bulk. Moreover, the perovskite film appears to be even more compact and smooth showing a distinct straight surface line of the upper bound. This result consolidates the proper choice of the ETL material as it appears to be morphologically compatible with the perovskite, not destructing the topography of the active layer.

In order to further investigate the morphology and roughness change after CsCl post-treatment of the pristine perovskite, top-view atomic force microscopy was conducted (Figure 11). In agreement with the SEM images, the AFM top view demonstrates an effect of the smoothness of the surface of perovskite bulk with additional particles appearing closer to the boundaries of the bulk crystals. These particles are also observable in SEM images as well. From the AFM-derived data, the root mean square (RMS) comparison was considered to numerically assess the roughness of the obtained films. The RMS of the pristine perovskite was equal to 0.143 μm, while the CsCl-treated surface produces RMS of 0.066 μm, which is more than 2 times improvement of the surface roughness towards smoothing after 10 seconds of CsCl tretament. This observation is important

for further evaluation of the perovskite film as a part of a solar cell device, since the smoother the surface the less likely the film would generate recombination sites at the interface between the active layer and hole-transporting layer.

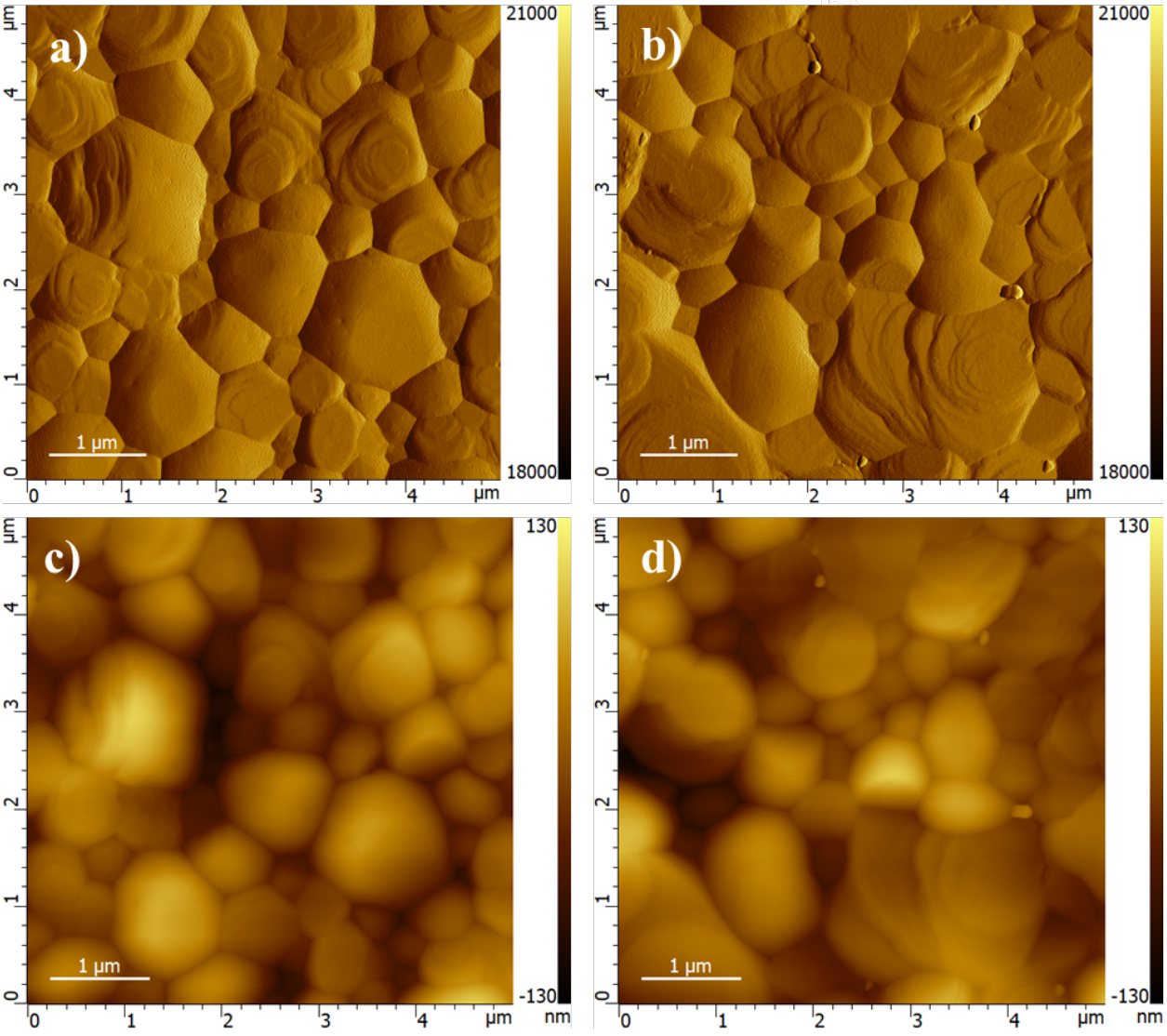

Figure 11. AFM images of top view on $CsPbI_2Br$ perovskite crystal (a,c) without and (b,d) with CsCl post-treatment (10 sec).

4.2 X-Ray Diffraction (XRD)

X-ray diffraction (XRD) analysis shows the information of the crystal lattice of the obtained pristine and CsCl-treated perovskites on FTO-glass substrate (Figure 12). There are three

intense peaks which are associated with the (100), (110) and (200) planes of the $CsPbI_2Br$ perovskites at 15.5°, 21.8°, and 30.4° respectively. In order to observe peak shifts associated with the CsCl post-treatment, Figure 12b-d shows each diffraction peak individually with the degree of the shift indicated. There is an obvious shift towards larger angles for $CsPbI_2Br$/CsCl film by 0.01°-0.03°. This effect is observed in crystal lattices as a result of a lattice contraction taking place, and in this system of materials the lattice shrinkage can be associated with the possible partial replacement of larger I^- or Br^- ions with smaller Cl^- ions.

There is also enhancement of the intensity of perovskite-characteristic peaks evident from Figure 12, and no peaks associated with phase degradation appear, which overall serves as a marker of the stability of the perovskite phase. The crystallinity of the perovskite film was calculated from the diffraction patterns, and the value for the $CsPbI_2Br$ perovskite was equal to 46.98%, while the CsCl-treatment improves the crystallinity up to 57.06%. This is a favorable improvement for solar cell applications especially in terms of low trap, defect density and minimal structural disorders within the crystal planes.

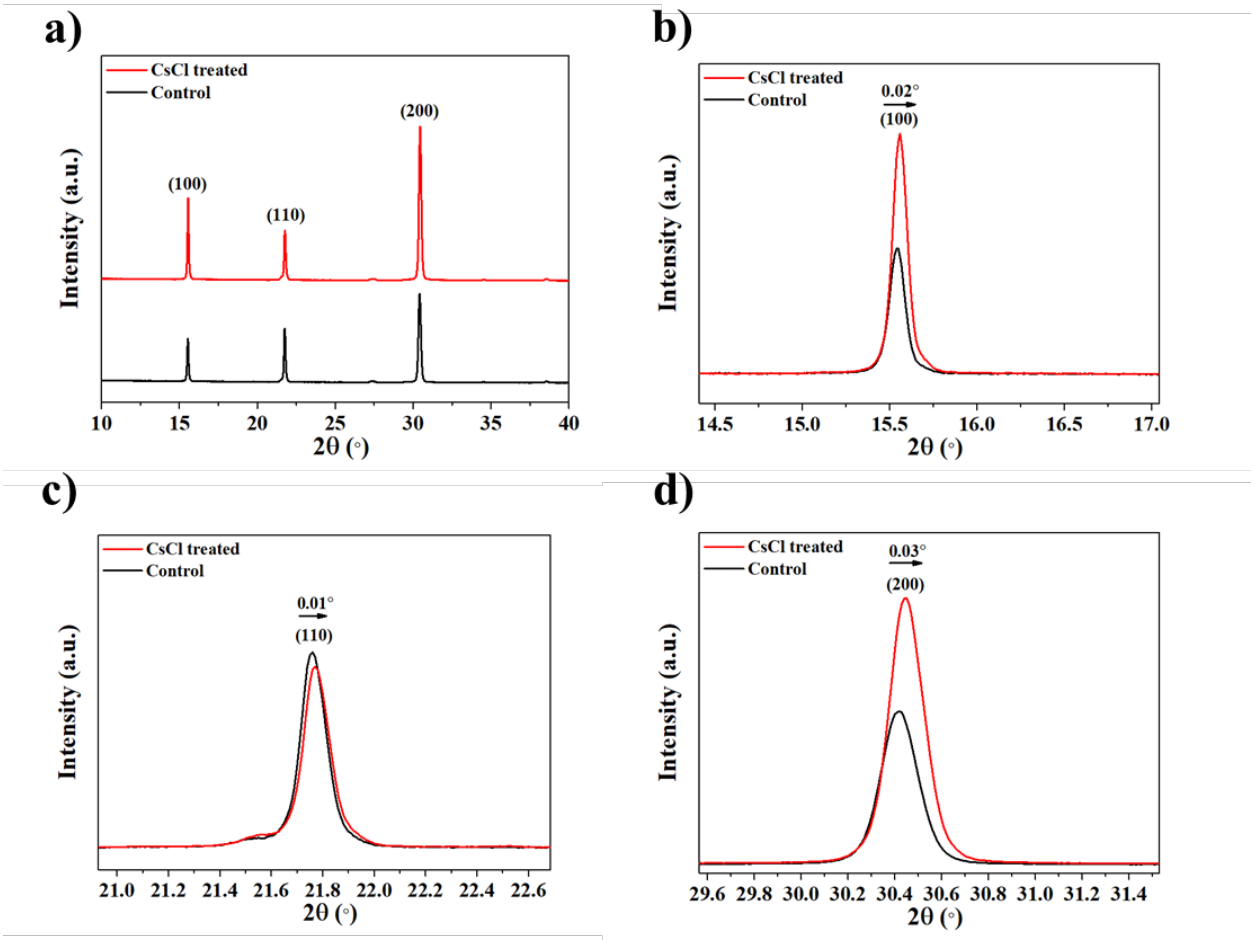

Figure 12. (a) XRD patterns and individual crystallographic peaks of $CsPbI_2Br$ perovskite thin film with and without CsCl treatment at (b) (100), (c) (110), and (d) (200) planes.

4.3 Photoluminescence Spectroscopy (PL)

In order to study the carrier recombination phenomena of perovskite with and without CsCl treatment, a steady-state photoluminescence was conducted. The peaks with the maximum intensity appear at 667 nm for the pristine $CsPbI_2Br$, and 658 nm for the CsCl-treated sample (Figure 13). From the PL spectra obtained for control perovskite and perovskite treated with CsCl, there is an obvious intensity increase after the sample is treated with CsCl, which may indicate the higher carrier density, low defect density and suppression of nonradiative recombination. Additionally, a slight blushift of 9 nm is observed on the PL spectra after CsCl treatment, which may be attributed to the slight Cl^- integration into the bulk of the perovskite, and subsequent band gap change from shorter to wider. This result is also consistent with the UV-Vis-derived data,

which shows the slight broadening of the E_g. In a 3D perovskite, the crystal structure consists of a continuous three-dimensional network formed by corner-sharing BX_6 octahedra. This continuous network facilitates strong orbital overlap between the metal cation B and the halide anions X, which leads to the formation of a bonding and an antibonding state (valence and conduction bands, respectively). The efficient orbital overlap and the continuous nature of the 3D perovskite structure result in a delocalized electronic structure across the entire lattice. Overall, it leads to a smaller energy difference between the valence and conduction bands, which results in a reduced or narrower bandgap observed for 3D perovskites. Conversely, 2D perovskites possess a stratified configuration where inorganic layers are interspersed with spacer cation Cs^+. Thus, in 2D perovskites, the electronic structure is localized due to the quantum confinement imposed by the spacers on the inorganic layers. The quantum confinement effect results in a broader bandgap when compared to 3D perovskites, therefore shifts in PL can be observed towards shorter wavelengths. However, for further confirmation of the PL peaks characteristic to 2D perovskite, there should be a broader range of wavelengths observed since the characteristic peaks may appear at the shorter wavelengths (350-500 nm) and with broad tails due to the self-trapped excitons [55]. Overall, the mentioned intensity change and blueshifting of the most intense peak for Cs-perovskite within the given range suggests the low-defect density trend after CsCl treatment, and SEM and AFM images give hints on the surface favorable modification attributed to the CsCl post-treatment.

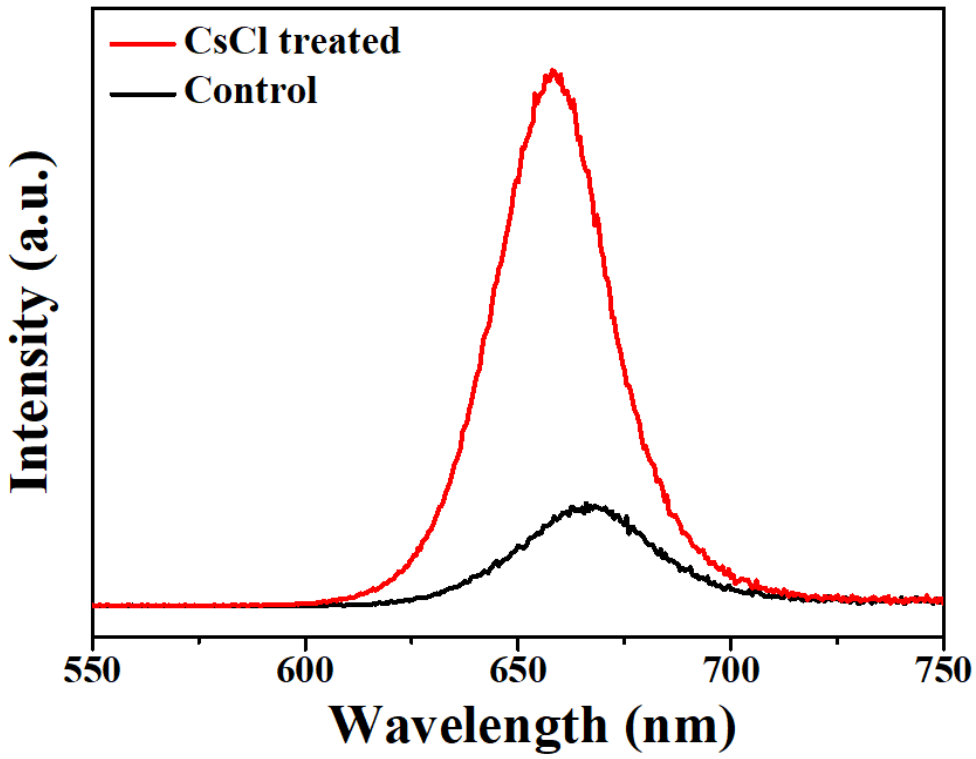

Figure 13. Steady-state photoluminescence (PL) spectra of the $CsPbI_2Br$ perovskite with and without CsCl post-treatment.

4.4 UV-Vis Absorption Spectroscopy (UV-Vis)

The UV-Vis absorption was studied in order to find the absorption properties of perovskite within a range of 500-800 nm of visible light spectrum (Figure 14). The pristine perovskite shows the absorption onset at 627.4 nm, and for CsCl-treated perovskite it is at 624.5 nm with a slight blueshift from the former by 2.9 nm. This blueshift is observed also in the reference article of H. Wang *et al*., where the CsCl treatment of the $CsPbI_3$ perovskites shifted the onset from 741 nm to 735 nm. The Tauc plot was obtained to evaluate the optical bandgap of the samples. There is a slight E_g increase from 1.88 eV to 1.89 eV evident after the CsCl treatment, which is also in agreement with the PL blueshift. From these results, it can be concluded that the optical absorption properties are changed slightly after the CsCl post-treatment, which can be related to the crystal lattice shrinkage and crystallinity increase observed in the XRD results. Additionally, the bandgap

shift from UV-Vis and PL can be then associated with the formation of new structures confirmed from the SEM and AFM images.

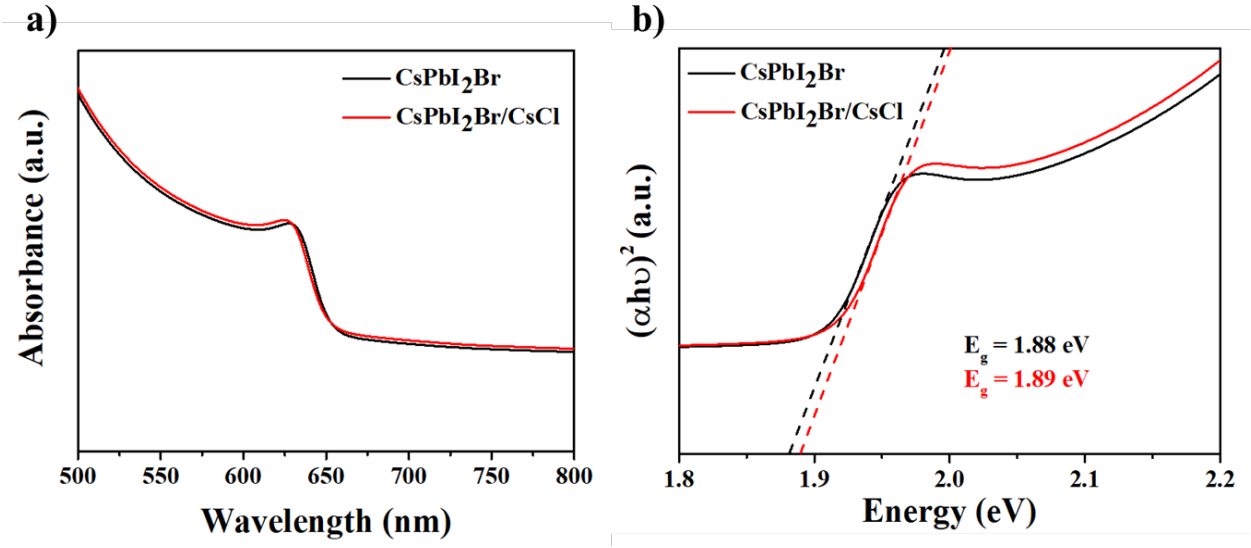

Figure 14. (a) UV-Vis absorption spectra and (b) Tauc plot with calculated E_g of the $CsPbI_2Br$ perovskite before and after CsCl post-treatment.

Although the bandgap changes are subtle, they are evident according to the analysis in the perovskite bulk, while there are important SEM and AFM observations to consider on the surface level of the perovskite after CsCl treatment. Therefore the XPS analysis was conducted additionally to study 10 nm-level chemical state changes.

4.5 X-Ray Photoelectron Spectroscopy (XPS)

X-ray photoelectron spectroscopy (XPS) was used to study the chemical state of $CsPbI_2Br$ perovskite together with the influence of CsCl treatment on the chemical state (Figure 15). The XPS results in Figure 15 confirm the incorporation of Cl^- ions in $CsPbI_2Br$ film after CsCl treatment (Figure 15a). The XPS technique is sensitive to the surface changes since the probe is analyzing the thin films up to 10 nm deep. From this information and Figure 15e, it is evident that the Cl^- is accumulated on the surface. At the same time, after the CsCl treatment the XPS peak positions for all elements Pb 4f were shifted towards higher binding energies (Figure 15b). This trend towards higher binding energies is also evident in the work of H. Wang *et al*. [36], where the

research group treated $CsPbI_3$ perovskite with CsX (where X - Cl, F, Br). In agreement with the reference article, there are shifts of Pb 4f towards higher binding energy after CsCl post-treatment as well, which is explained by the orbital interactions between Pb 4f and Cl 3d orbitals in the CsCl treated samples. Compared to I^- and Br^-, Cl^- has smaller atomic size, and more effective nuclear charge on the valence electrons, thus it would have more effective overlap with Pb^+, resulting in stronger bonding between Cl and Pb, which shifts the XPS peaks towards higher binding energies of Pb 4f. This observation is also in agreement with the discussion on the XRD peak shifts due to lattice shrinkage, which was associated with the intrusion of Cl^- into the perovskite. It can be deduced from the chemical state from XPS, lattice deformations from XRD and morphology changes from SEM measurements, that the introduction of Cl^- from CsCl structurally change perovskite surface and induce the formation of new needle-shaped structures, which has different dimensionality compared to the 3D perovskite bulk.

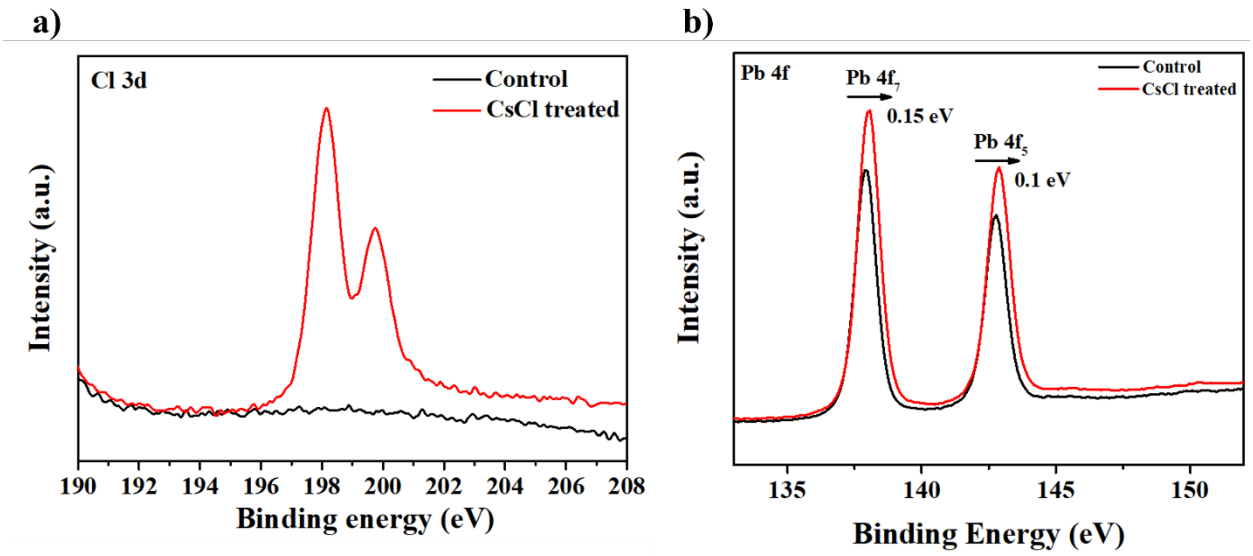

Figure 15. XPS spectra of $CsPbI_2Br$ perovskite with and without CsCl treatment of (a) Cl 3d and (b) Pb 4f.

4.6 Device Characterization

The performance of the champion devices was evaluated using current density versus voltage, external quantum efficiency, current density versus time and stability measurements (Figure 16).

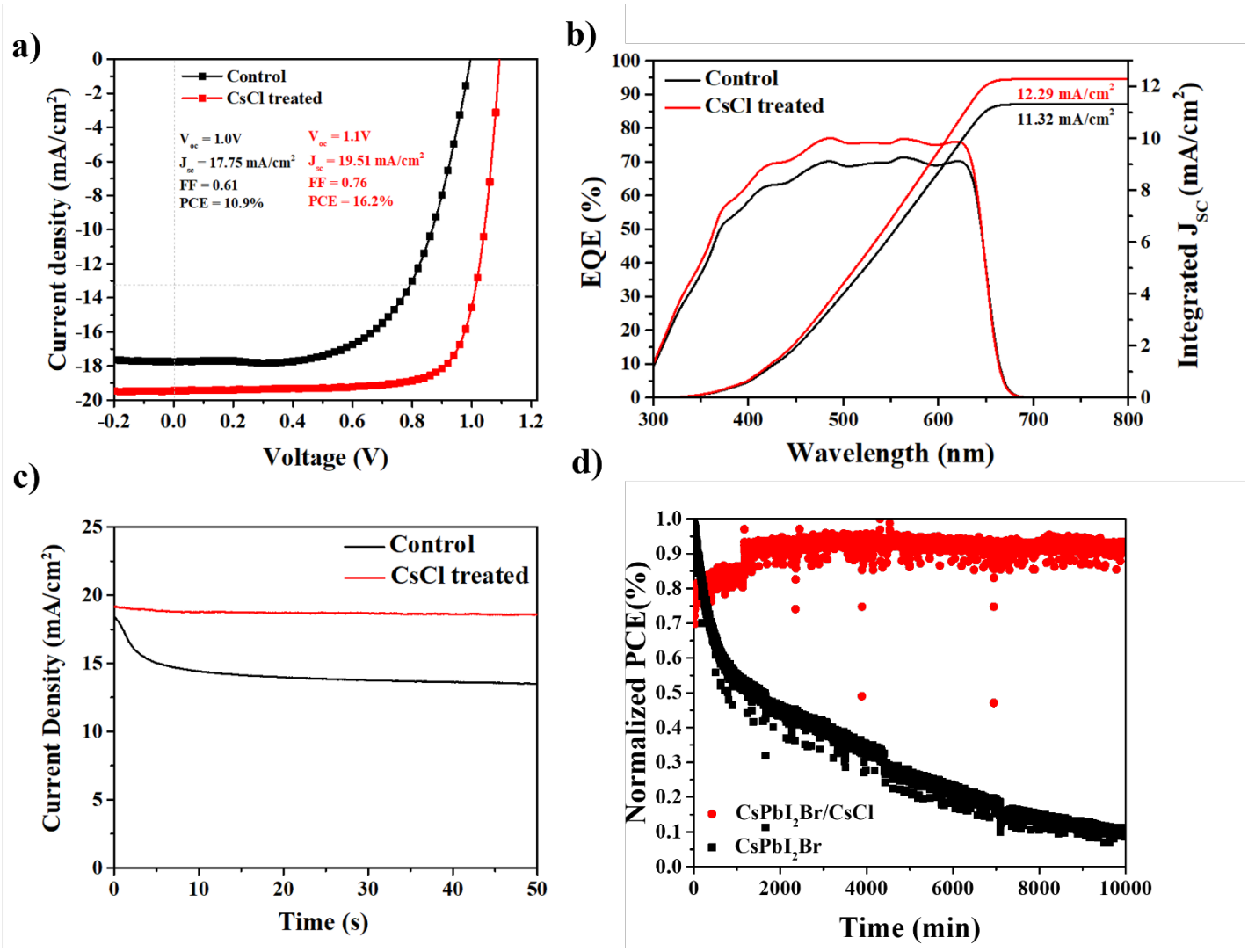

Figure 16. PSC characteristics with control perovskite and perovskite post-treated with CsCl: (a) forward scanned J-V curves, (b) EQE with integrated J_{SC}, (c) I-t scan during 50 seconds, (d) Stability test during 7 days at RH=20%.

The effect of CsCl treatment on the photovoltaic performance of solar cells is evaluated by collecting data of 7 devices for each condition and comparing the PV parameters with each other (Table 2). In Table 2 the photovoltaic performance is demonstrated in terms of the V_{OC}, J_{SC}, FF, and PCE values. The statistical box plots of the photovoltaic parameters are additionally represented in Figure 17. While V_{OC} is similar for both conditions being around 1.08 V, the *Jsc* value is much increased after CsCl treatment. A higher J_{SC} indicates that the PSC with CsCl post-treatment (19.01 mA/cm²) generates more photocurrent than the control sample (16.04 mA/cm²)

under the same light conditions. This higher photocurrent may be attributed to various factors or their combination such as improved light absorption, more efficient charge carrier generation, and better charge separation within the solar cell. Another parameter is a fill factor, which is also improved after CsCl post-treatment. The FF value of 66.12±7.00 indicates that the PSC after CsCl treatment is operating more efficiently compared to the control PSC (FF = 61.00±4.18). Overall, PSC after CsCl has a better quality I-V curve, lower internal resistive losses, and more efficient charge extraction compared to the control one. In agreement with the improved photovoltaic parameters such as J_{SC} and FF, the power conversion efficiency (PCE) is also increased from 10.6±1.49% of a pristine $CsPbI_2Br$ perovskite to 13.50±1.46% after treatment with CsCl, with the champion device showing PCE of 16.2% (Figure 16a).

Table 2. PSC performance of control and CsCl-treated devices based on J-V measurements averaged to 7 devices.

		V_{OC} (V)	**J_{SC} (mA/cm^2)**	**FF**	**PCE (%)**
Control	Forward	1.08±0.03	16.04±2.02	61.00±4.18	10.60±1.49
	Reverse	0.93±0.08	15.53±2.1	44.88±8.82	6.52±1.86
With CsCl treatment	Forward	1.08±0.04	19.01±2.13	66.12±7.00	13.50±1.46
	Reverse	0.95±0.05	18.86±2.13	51.58±7.07	9.20±1.67

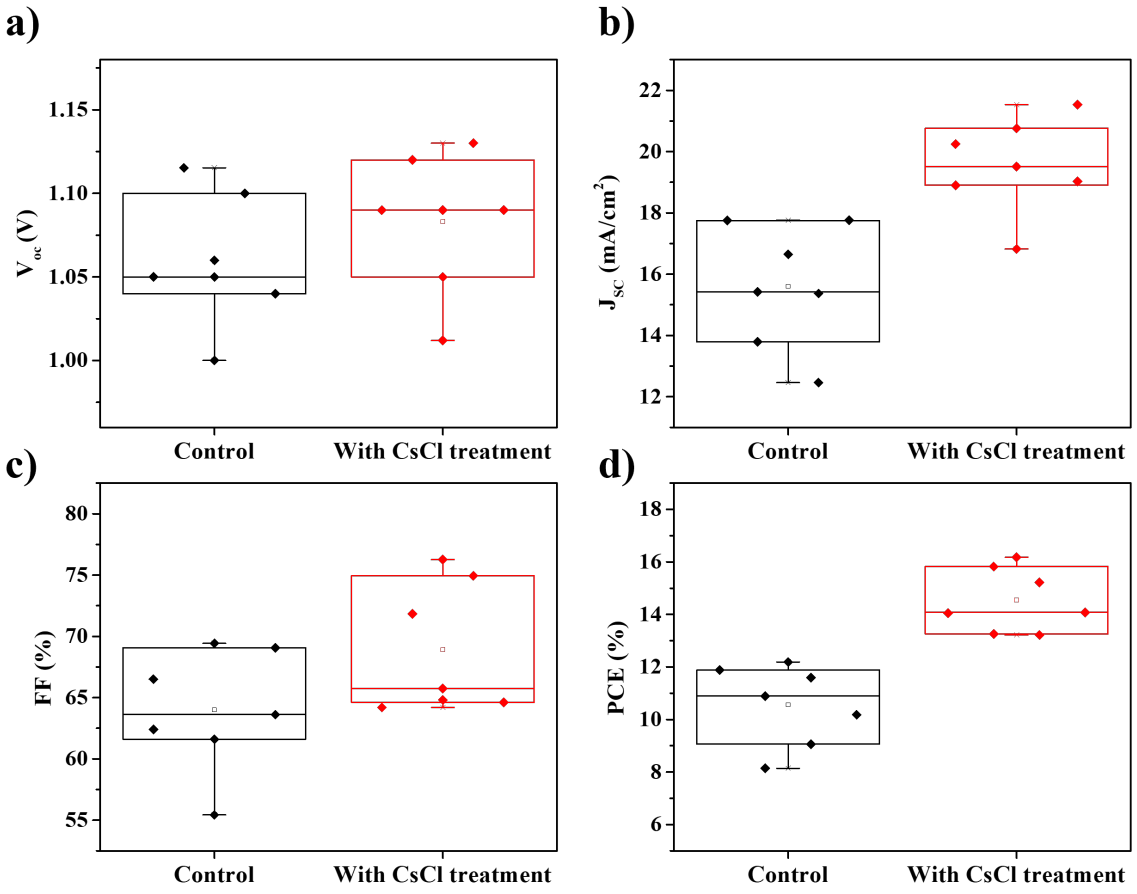

Figure 17. Box plots of the photovoltaic parameters of the perovskite solar cells obtained before and after CsCl post-treatment: (a) Open-circuit voltage (V_{OC}), (b) short-circuit current density (J_{SC}), (c) fill factor (FF), and (d) power conversion efficiency (PCE).

The external quantum efficiency (EQE) was measured for the samples and are shown in Figure 16b. The comparison of EQE measurements showed that there is an improvement in the EQE response of the device after CsCl post-treatment. It is an indication that for CsCl-treated samples the percentage of incident photons that generate an electron-hole pair (exciton), which can then be separated and collected as electrical current, is higher than that of the control sample. It can be attributed to the more stabilized perovskite photoactive phases, which was observed in XRD spectra, therefore more light fraction can be absorbed with the potential to create excitons. The integrated current densities estimated from the EQE spectra are equal to 12.29 mA/cm^2 and 11.32 mA/cm^2 for the CsCl treated and control PSCs respectively, which are lower compared to the

reported from the IV-measurements. Typically, when low-intensity monochromatic light is utilized during the external quantum efficiency measurements, PSCs encounter an elevated photocurrent barrier. However, this effect is less prominent when the solar cells are exposed to the intense illumination from a solar simulator. Consequently, the integrated J_{SC} derived from the EQE measurements are likely underestimated.

The stabilized current density at the maximum power point is shown in the Figure 16c, with the applied voltage of 0.84V. The obtained results show the improvement of the stabilized power output of the CsCl-PSCs, while there is an abrupt and consistent decay of the current density for the control PSC during the 50 seconds measuring time under light illumination. The stabilized J_{SC} of Figure 16c is in agreement with the statistical average of the J_{SC} values presented in Table 2, 16.04±2.02 mA/cm^2 against 19.01±2.13 mA/cm^2.

To finally evaluate the lifetime of the PSCs with and without CsCl treatment, the normalized photovoltaic performance of the champion PSC devices was measured during 7 days under relative humidity of 20% (Figure 16d). According to the obtained photovoltaic aging test results, the control device is significantly degraded producing lower PCE with time, while the performance of the CsCl-treated samples is more stable within the same period. This observation suggests the significant improvement of resistance to ambient conditions due to the CsCl treatment methodology.

Conclusion

In conclusion, this work has successfully addressed the challenges associated with conventional hybrid 3D perovskites for photovoltaic applications, which suffer from fast degradation due to weak moisture and thermal stability. By focusing on Cs-based perovskites and employing multidimensional engineering, the work has demonstrated a promising solution to enhance ambient stability. The aims were achieved by first obtaining uniform polycrystalline perovskite bulk through the synthesis of high-crystalline Cs-based 3D-perovskites and then incorporating CsCl to create multidimensional structures, where Cs^+ served as a spacer cation. These optimized materials formed the basis for fabricating high-performance photovoltaic devices.

Morphological and topographical properties of the perovskite were analyzed through SEM and AFM, revealing a smooth surface morphology, low defect density, large grain size, and uniform surface coverage, which are essential factors for enhancing the power conversion efficiency of PSCs. Meanwhile, the CsCl treatment introduced morphological changes in the form of nanoneedle-shaped structures, without affecting the compatibility between the ETL and perovskite layers. The obtained structures are more pronounced upon longer treatment with CsCl solution, and are associated with the 2D perovskites. At the same time, treatment for 10 seconds only can significantly improve the surface roughness, as assessed by RMS values, indicating the potential for further optimization of perovskite-based solar cells. XRD analysis showed lattice contraction, increased intensity of perovskite-characteristic peaks, and improved crystallinity upon CsCl treatment, giving the hints on possible Cl^- incorporation into the $CsPbI_2Br$ lattice. This was confirmed by analyzing the XPS, which also demonstrated Cl^- appearance and chemical shifts associated with stronger Pb-Cl bonding. The induced morphological changes as well as the chemical rearrangement of the ions further solidifies the idea of 2D perovskites formation upon CsCl treatment. Steady-state PL and UV-Vis absorption demonstrated subtle bandgap changes and shifts in accordance to the typical effect of widening bandgap of 2D structures. Overall, the obtained results hint at the formation of the 2D-perovskites within the $CsPbI_2Br$ 3D perovskite bulk. Further investigations of the obtained nanoneedle-structures are planned in order to establish their nature thoroughly.

By now the positive effect of the newly obtained structures can be assessed in terms of the performance of the solar cells, which is improved by following the CsCl-treatment method for 10 seconds. The PCE increased from 10.60±1.49% to 13.50±1.46%, and maintained the stable performance during 7 days at 20% of RH. Other characteristics such as FF, J_{SC}, and EQE also showed improvement towards higher values. These observations create more space to drive forward the Cs-based perovskite interfacial modification techniques, creating multidimensional structures by the facile method of CsCl post-treatment developed in this work.

Bibliography

[1] A. Chilvery, S. Das, P. Guggilla, C. Brantley, and A. Sunda-Meya, "A perspective on the recent progress in solution-processed methods for highly efficient perovskite solar cells," *Sci Technol Adv Mater*, vol. 17, no. 1, pp. 650–658, Jan. 2016, doi: 10.1080/14686996.2016.1226120.

[2] W. Chen, X. Li, Y. Li, and Y. Li, "A review: crystal growth for high-performance all-inorganic perovskite solar cells," *Energy Environ Sci*, vol. 13, no. 7, pp. 1971–1996, 2020, doi: 10.1039/D0EE00215A.

[3] Q. Dong *et al.*, "Electron-hole diffusion lengths > 175 μm in solution-grown $CH_3NH_3PbI_3$ single crystals," *Science (1979)*, vol. 347, no. 6225, 2015, doi: 10.1126/science.aaa5760.

[4] G. Nazir *et al.*, "Stabilization of Perovskite Solar Cells: Recent Developments and Future Perspectives," *Advanced Materials*, vol. 34, no. 50. 2022. doi: 10.1002/adma.202204380.

[5] M. A. Green *et al.*, "Solar cell efficiency tables (version 50)," *Progress in Photovoltaics: Research and Applications*, vol. 25, no. 7, 2017, doi: 10.1002/pip.2909.

[6] Y. Liu *et al.*, "Ultrahydrophobic 3D/2D fluoroarene bilayer-based water-resistant perovskite solar cells with efficiencies exceeding 22%," *Sci Adv*, vol. 5, no. 6, 2019, doi: 10.1126/sciadv.aaw2543.

[7] J. Tian, Q. Xue, Q. Yao, N. Li, C. J. Brabec, and H. L. Yip, "Inorganic Halide Perovskite Solar Cells: Progress and Challenges," *Advanced Energy Materials*, vol. 10, no. 23. 2020. doi: 10.1002/aenm.202000183.

[8] J. Wang *et al.*, "Highly efficient all-inorganic perovskite solar cells with suppressed non-radiative recombination by a Lewis base," *Nat Commun*, vol. 11, no. 1, p. 177, 2020, doi: 10.1038/s41467-019-13909-5.

[9] B. Wang, N. Novendra, and A. Navrotsky, "Energetics, Structures, and Phase Transitions of Cubic and Orthorhombic Cesium Lead Iodide ($CsPbI_3$) Polymorphs," *J Am Chem Soc*, vol. 141, no. 37, pp. 14501–14504, Sep. 2019, doi: 10.1021/jacs.9b05924.

[10] J. Liang *et al.*, "All-Inorganic Perovskite Solar Cells," *J Am Chem Soc*, vol. 138, no. 49, pp. 15829–15832, Dec. 2016, doi: 10.1021/jacs.6b10227.

[11] S. Mariotti, O. S. Hutter, L. J. Phillips, P. J. Yates, B. Kundu, and K. Durose, "Stability and Performance of CsPbI2Br Thin Films and Solar Cell Devices," *ACS Appl Mater Interfaces*, vol. 10, no. 4, pp. 3750–3760, Jan. 2018, doi: 10.1021/acsami.7b14039.

[12] T. Ozturk, E. Akman, A. E. Shalan, and S. Akin, "Composition engineering of operationally stable CsPbI2Br perovskite solar cells with a record efficiency over 17%," *Nano Energy*, vol. 87, 2021, doi: 10.1016/j.nanoen.2021.106157.

[13] Y. Haruta, T. Ikenoue, M. Miyake, and T. Hirato, "One-Step Coating of Full-Coverage CsPbBr3Thin Films via Mist Deposition for All-Inorganic Perovskite Solar Cells," *ACS Appl Energy Mater*, vol. 3, no. 12, 2020, doi: 10.1021/acsaem.0c01985.

[14] Q. Yuan *et al.*, "Thermally Stable Perovskite Solar Cells by All-Vacuum Deposition," *ACS Appl Mater Interfaces*, 2022, doi: 10.1021/acsami.2c14658.

[15] A. Ng *et al.*, "Crystal Engineering for Low Defect Density and High Efficiency Hybrid Chemical Vapor Deposition Grown Perovskite Solar Cells," *ACS Appl Mater Interfaces*, vol. 8, no. 48, 2016, doi: 10.1021/acsami.6b07513.

[16] D. Burkitt *et al.*, "Roll-to-roll slot-die coated P-I-N perovskite solar cells using acetonitrile based single step perovskite solvent system," *Sustain Energy Fuels*, vol. 4, no. 7, 2020, doi: 10.1039/d0se00460j.

[17] M. Mangrulkar and K. J. Stevenson, "The progress of additive engineering for $CH_3NH_3PbI_3$ photo-active layer in the context of perovskite solar cells," *Crystals*, vol. 11, no. 7. 2021. doi: 10.3390/cryst11070814.

[18] D. Aidarkhanov *et al.*, "Passivation engineering for hysteresis-free mixed perovskite solar cells," *Solar Energy Materials and Solar Cells*, vol. 215, p. 110648, 2020, doi: https://doi.org/10.1016/j.solmat.2020.110648.

[19] A. Maiti, S. Chatterjee, L. Peedikakkandy, and A. J. Pal, "Defects and Their Passivation in Hybrid Halide Perovskites toward Solar Cell Applications," *Solar RRL*, vol. 4, no. 12. 2020. doi: 10.1002/solr.202000505.

[20] B. Li *et al.*, "Surface passivation engineering strategy to fully-inorganic cubic $CsPbI_3$ perovskites for high-performance solar cells," *Nat Commun*, vol. 9, no. 1, 2018, doi: 10.1038/s41467-018-03169-0.

[21] T. Zhang *et al.*, "Bication lead iodide 2D perovskite component to stabilize inorganic a-$CsPbI_3$ perovskite phase for high-efficiency solar cells," *Sci Adv*, vol. 3, no. 9, 2017, doi: 10.1126/sciadv.1700841.

[22] M. A. Green, A. Ho-Baillie, and H. J. Snaith, "The emergence of perovskite solar cells," *Nature Photonics*, vol. 8, no. 7. 2014. doi: 10.1038/nphoton.2014.134.

[23] W. Huang, T. Bu, F. Huang, and Y.-B. Cheng, "Stabilizing High Efficiency Perovskite Solar Cells with 3D-2D Heterostructures," *Joule*, vol. 4, no. 5, pp. 975–979, 2020, doi: https://doi.org/10.1016/j.joule.2020.04.009.

[24] Y. Chen, S. Yu, Y. Sun, and Z. Liang, "Phase Engineering in Quasi-2D Ruddlesden–Popper Perovskites," *J Phys Chem Lett*, vol. 9, no. 10, pp. 2627–2631, May 2018, doi: 10.1021/acs.jpclett.8b00840.

[25] Y. Liu *et al.*, "Ultrahydrophobic 3D/2D fluoroarene bilayer-based water-resistant perovskite solar cells with efficiencies exceeding 22%," *Sci Adv*, vol. 5, no. 6, p. eaaw2543, Oct. 2022, doi: 10.1126/sciadv.aaw2543.

[26] Y. Cho *et al.*, "Mixed 3D–2D Passivation Treatment for Mixed-Cation Lead Mixed-Halide Perovskite Solar Cells for Higher Efficiency and Better Stability," *Adv Energy Mater*, vol. 8, no. 20, p. 1703392, Jul. 2018, doi: https://doi.org/10.1002/aenm.201703392.

[27] Y. Wang, T. Zhang, M. Kan, Y. Li, T. Wang, and Y. Zhao, "Efficient α-CsPbI3 Photovoltaics with Surface Terminated Organic Cations," *Joule*, vol. 2, no. 10, pp. 2065–2075, 2018, doi: https://doi.org/10.1016/j.joule.2018.06.013.

[28] T. Liu *et al.*, "Modifying Surface Termination of $CsPbI_3$ Grain Boundaries by 2D Perovskite Layer for Efficient and Stable Photovoltaics," *Adv Funct Mater*, vol. 31, no. 15, p. 2009515, Apr. 2021, doi: https://doi.org/10.1002/adfm.202009515.

[29] J. Li *et al.*, "Bottom-up passivation effects by using 3D/2D mix structure for high performance p-i-n perovskite solar cells," *Solar Energy*, vol. 205, pp. 44–50, 2020, doi: https://doi.org/10.1016/j.solener.2020.05.042.

[30] T. M. Koh *et al.*, "Enhancing moisture tolerance in efficient hybrid 3D/2D perovskite photovoltaics," *J Mater Chem A Mater*, vol. 6, no. 5, pp. 2122–2128, 2018, doi: 10.1039/C7TA09657G.

[31] M. K. A. Mohammed, A. Esmail Shalan, M. Dehghanipour, and H. R. Mohseni, "Improved mixed-dimensional 3D/2D perovskite layer with formamidinium bromide salt for highly

efficient and stable perovskite solar cells," *Chemical Engineering Journal*, vol. 428, p. 131185, 2022, doi: https://doi.org/10.1016/j.cej.2021.131185.

[32] K. Wang *et al.*, "Ruddlesden–Popper 2D Component to Stabilize γ-$CsPbI_3$ Perovskite Phase for Stable and Efficient Photovoltaics," *Adv Energy Mater*, vol. 9, no. 42, p. 1902529, Nov. 2019, doi: https://doi.org/10.1002/aenm.201902529.

[33] S. Zhang *et al.*, "Spontaneous Construction of Multidimensional Heterostructure Enables Enhanced Hole Extraction for Inorganic Perovskite Solar Cells to Exceed 20% Efficiency," *Adv Energy Mater*, vol. 12, no. 1, p. 2103007, Jan. 2022, doi: https://doi.org/10.1002/aenm.202103007.

[34] Q. Li *et al.*, "Interfacial Engineering by In Situ Building of a 3D/2D Heterojunction for Inverted $CsPbI_2Br$ Solar Cells: Beyond Moisture Proof," *ACS Appl Energy Mater*, vol. 4, no. 9, pp. 10081–10090, Sep. 2021, doi: 10.1021/acsaem.1c02005.

[35] J.-X. Song, X.-X. Yin, Z.-F. Li, and Y.-W. Li, "Low-temperature-processed metal oxide electron transport layers for efficient planar perovskite solar cells," *Rare Metals*, vol. 40, no. 10, pp. 2730–2746, 2021, doi: 10.1007/s12598-020-01676-y.

[36] H. Wang *et al.*, "Size mismatch induces cation segregation in $CsPbI_3$: Forming energy level gradient and 3D/2D heterojunction promotes the efficiency of carbon-based perovskite solar cells to over 15%," *Nano Energy*, vol. 89, p. 106411, 2021, doi: https://doi.org/10.1016/j.nanoen.2021.106411.

[37] S. Yang *et al.*, "2D $Cs_2PbI_2Cl_2$ Nanosheets for Holistic Passivation of Inorganic $CsPbI_2Br$ Perovskite Solar Cells for Improved Efficiency and Stability," *Adv Energy Mater*, vol. 10, no. 46, p. 2002882, Dec. 2020, doi: https://doi.org/10.1002/aenm.202002882.

[38] X. Jiang *et al.*, "Dion-Jacobson 2D-3D perovskite solar cells with improved efficiency and stability," *Nano Energy*, vol. 75, p. 104892, 2020, doi: https://doi.org/10.1016/j.nanoen.2020.104892.

[39] Yukta, N. Parikh, R. D. Chavan, P. Yadav, M. K. Nazeeruddin, and S. Satapathi, "Highly Efficient and Stable 2D Dion Jacobson/3D Perovskite Heterojunction Solar Cells," *ACS Appl Mater Interfaces*, vol. 14, no. 26, pp. 29744–29753, Jul. 2022, doi: 10.1021/acsami.2c04455.

[40] W. Li, X. Gu, C. Shan, X. Lai, X. W. Sun, and A. K. K. Kyaw, "Efficient and stable mesoscopic perovskite solar cell in high humidity by localized Dion-Jacobson 2D-3D

heterostructures," *Nano Energy*, vol. 91, p. 106666, 2022, doi: https://doi.org/10.1016/j.nanoen.2021.106666.

[41] "Schematic of perovskite solar cell." Okinawa Institute of Science and Technology. https://www.oist.jp/image/schematic-perovskite-solar-cell (accessed Mar. 16, 2023).

[42] M. Yu *et al.*, "Power output and carrier dynamics studies of perovskite solar cells under working conditions," *Physical Chemistry Chemical Physics*, vol. 19, no. 30, 2017, doi: 10.1039/c7cp02715j.

[43] A. K. Chandiran, M. Abdi-Jalebi, M. K. Nazeeruddin, and M. Grätzel, "Analysis of electron transfer properties of ZnO and TiO_2 photoanodes for dye-sensitized solar cells," *ACS Nano*, vol. 8, no. 3, 2014, doi: 10.1021/nn405535j.

[44] P. Zhang *et al.*, "Perovskite Solar Cells with ZnO Electron-Transporting Materials," *Advanced Materials*, vol. 30, no. 3, 2018, doi: 10.1002/adma.201703737.

[45] J. Yang, B. D. Siempelkamp, E. Mosconi, F. De Angelis, and T. L. Kelly, "Origin of the Thermal Instability in $CH_3NH_3PbI_3$ Thin Films Deposited on ZnO," *Chemistry of Materials*, vol. 27, no. 12, pp. 4229–4236, Jun. 2015, doi: 10.1021/acs.chemmater.5b01598.

[46] C. Honsberg and S. Bowden. "Chapter 8. Characterization." Photovoltaics Education Website. https://www.pveducation.org/pvcdrom/characterisation/introduction (accessed Mar. 16, 2023).

[47] T. S. Sherkar *et al.*, "Recombination in Perovskite Solar Cells: Significance of Grain Boundaries, Interface Traps, and Defect Ions," *ACS Energy Lett*, vol. 2, no. 5, pp. 1214–1222, May 2017, doi: 10.1021/acsenergylett.7b00236.

[48] Dutrow Barbara L. and Clark Christine M., "X-ray Powder Diffraction (XRD)." Science Education Resource Center at Carleton College. https://serc.carleton.edu/research_education/geochemsheets/techniques/XRD.html (accessed Mar. 16, 2023).

[49] A. Nanakoudis, "What is SEM? Scanning Electron Microscopy Explained," ThermoFisher Scientific. https://www.thermofisher.com/blog/materials/what-is-sem-scanning-electron-microscopy-explained/. Nov. 14, 2019 (accessed Mar. 16, 2023).

[50] “AFM Principle - How Does an Atomic Force Microscope Work?” Oxford Instruments Asylum Research. https://afm.oxinst.com/outreach/how-does-an-afm-microscope-work (accessed Mar. 16, 2023).

[51] “X-ray photoelectron spectroscopy: Principle, instrumentation, application,” Chemist Notes. https://chemistnotes.com/physical/x-ray-photoelectron-spectroscopy-principle-instrumentation-application/. May 18, 2022 (accessed Mar. 16, 2023).

[52] “Photoluminescence Spectroscopy.” Ossila. https://www.ossila.com/pages/photoluminescence (accessed Mar. 16, 2023).

[53] T. Justin, “UV-Vis Spectroscopy: Principle, Strengths and Limitations and Applications,” Jun. 30, 2021.

[54] M. Z. Farah Khaleda, B. Vengadaesvaran, and N. A. Rahim, “Spectral response and quantum efficiency evaluation of solar cells: A review,” in *Energy Materials: Fundamentals to Applications*, 2021. doi: 10.1016/B978-0-12-823710-6.00014-5.

[55] O. Nazarenko, M. R. Kotyrba, M. Wörle, E. Cuervo-Reyes, S. Yakunin, and M. V. Kovalenko, “Luminescent and Photoconductive Layered Lead Halide Perovskite Compounds Comprising Mixtures of Cesium and Guanidinium Cations,” *Inorg Chem*, vol. 56, no. 19, 2017, doi: 10.1021/acs.inorgchem.7b01204.